JACS
JOURNAL OF THE AMERICAN CHEMICAL SOCIETY
pubs.acs.org/JACS

Article

Displacive Jahn−Teller Transition in $NaNiO_2$

Liam A. V. Nagle-Cocco,* Annalena R. Genreith-Schriever, James M. A. Steele, Camilla Tacconis, Joshua D. Bocarsly, Olivier Mathon, Joerg C. Neuefeind, Jue Liu, Christopher A. O'Keefe, Andrew L. Goodwin, Clare P. Grey, John S. O. Evans, and Siân E. Dutton*

Cite This: J. Am. Chem. Soc. 2024, 146, 29560−29574

Read Online

ACCESS | Metrics & More | Article Recommendations | Supporting Information

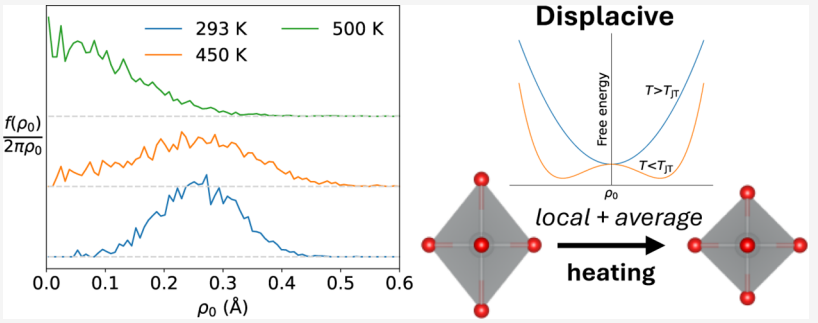

ABSTRACT: Below its Jahn−Teller transition temperature, T_{JT}, $NaNiO_2$ has a monoclinic layered structure consisting of alternating layers of edge-sharing NaO_6 and Jahn−Teller-distorted NiO_6 octahedra. Above T_{JT} where $NaNiO_2$ is rhombohedral, diffraction measurements show the absence of a cooperative Jahn−Teller distortion, accompanied by an increase in the unit cell volume. Using neutron total scattering, solid-state Nuclear Magnetic Resonance (NMR), and extended X-ray absorption fine structure (EXAFS) experiments as local probes of the structure we find direct evidence for a displacive, as opposed to order−disorder, Jahn−Teller transition at T_{JT}. This is supported by *ab initio* molecular dynamics (AIMD) simulations. To our knowledge this study is the first to show a displacive Jahn−Teller transition in any material using direct observations with local probe techniques.

1. INTRODUCTION

In an undistorted octahedrally coordinated environment, partially occupied e_g orbitals in a transition metal cation would be degenerate and therefore unstable to symmetry-reducing distortions by the Jahn−Teller (JT) effect.[1] This lifts the degeneracy of both the t_{2g} and partially occupied e_g orbitals, lowering the energy of the system.[1−4] The resulting octahedral distortion is often a linear combination of two possible van Vleck modes:[5,6] a planar rhombic Q_2 distortion and a tetragonal Q_3 elongation/compression (Figure S1). Experimentally, the distortion is normally dominated by the Q_3 tetragonal elongation. This JT distortion, and associated orbital ordering, is relevant to many phenomena including unconventional superconductivity in the cuprates,[7,8] magnetic structure through coupling of spin and orbital ordering,[9] and ionic mobility,[10,11] and can lead to structural transitions in a material when it is used in a battery electrode.[10−12]

In a crystalline material, the energy of a JT-distorted system is often minimized when the axes of elongation of neighboring octahedra are correlated; this is termed a cooperative JT distortion, in contrast to a noncooperative system in which axes of elongation are randomly distributed.[4] Transitions from low-temperature, cooperative JT distortions to a high-temperature state with an undistorted average structure can generally be classified as order−disorder or displacive.[13] In the former case, noncooperative JT distortions persist locally but are averaged out in the bulk structure, whereas in the latter case the local structure is undistorted. This paradigm has been applied to several systems.[13−17] The best-studied is the JT-distorted d^4 Mn^{3+} perovskite $LaMnO_3$ which shows evidence for an order−disorder JT transition;[14,15,18,19] theoretical works[20−22] and total scattering experiments[16] indicate a transition to a Potts model[20] type of orbital disorder.

The order−disorder/displacive paradigm has also been applied to the layered transition metal oxides with formula AMO_2 (A=alkali metal, M=transition metal).[13,17] This family of materials includes several battery materials such as $LiNiO_2$, $NaNiO_2$, $LiMnO_2$, and $NaMnO_2$, all of which feature transition metal ions with degenerate d^7/d^4 configurations which are liable

Received: July 21, 2024
Revised: September 20, 2024
Accepted: September 27, 2024
Published: October 14, 2024

https://doi.org/10.1021/jacs.4c09922
J. Am. Chem. Soc. 2024, 146, 29560−29574

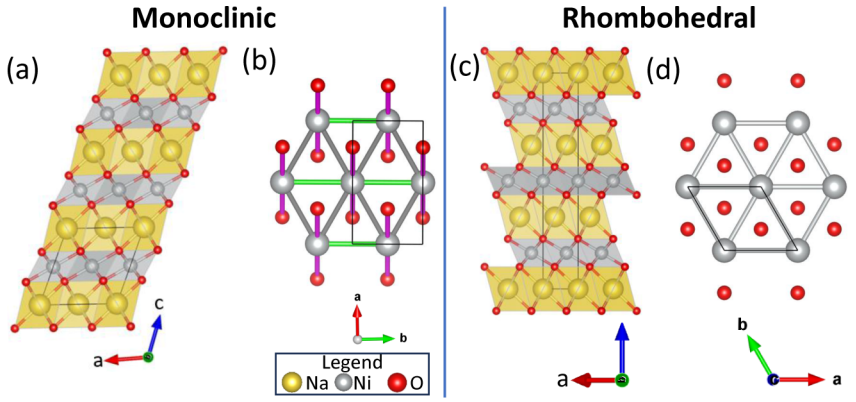

Figure 1. Crystal structures of (a) $C2/m$ monoclinic and (c) $R\bar{3}m$ rhombohedral $NaNiO_2$. (b) and (d) show the Ni−Ni distances (gray for nonelongated; green for elongated) and JT-elongated Ni−O distances (pink) in these two structures. In the rhombohedral structure there are no elongated Ni−Ni or Ni−O bonds.

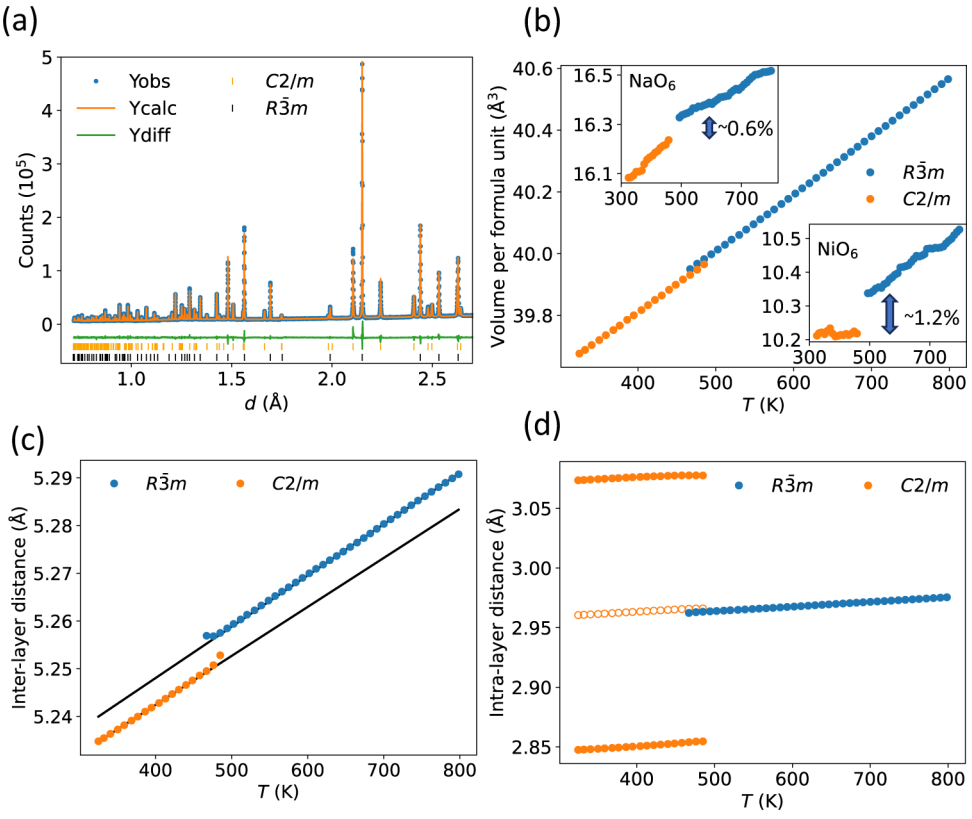

Figure 2. (a) Representative Rietveld refinement of synchrotron X-ray diffraction data for $NaNiO_2$ at 476.1 K in the mixed-phase regime where the rhombohedral ($R\bar{3}m$) and monoclinic ($C2/m$) phases coexist. (b) Volume per formula unit as a function of temperature, showing the slight increase in unit cell volume of the rhombohedral phase compared with the monoclinic phase. Insets are NaO_6 (top left) and NiO_6 (top right) octahedral volume with temperature, calculated using VanVleckCalculator;[6,45] only volumes in the single-phase regions are plotted. Temperature-dependence of the (c) interlayer distances, $c/3$ for the rhombohedral phase and $c\sin(\beta)$ for the monoclinic phase, and (d) intralayer distances, a for the rhombohedral phase, and $a/\sqrt{3}$ and b for the monoclinic phase. The intralayer distances correspond to the Ni−Ni and Na−Na distances within the plane. For the monoclinic phase, closed circles are the individual distances, open circles are averaged. In (c), points are experimental values obtained by Rietveld refinement, and solid lines are a linear fit. In (b,c,d) error bars are smaller than data points.

to JT distortions. The AMO_2 materials have layers of edge-sharing MO_6 octahedra forming a triangular network of M cations, separated by a layer of octahedrally coordinated alkali metal ions, in contrast to the perovskites such as $LaMnO_3$ which have corner-sharing octahedra and an approximately cubic cation network. The aristotype of the structure has rhombohedral $R\bar{3}m$ symmetry, but $NaNiO_2$ and each of α- and β-$XMnO_2$ (X = Li, Na) show cooperative JT ordering[13] resulting in a macroscopic distortion. $NaNiO_2$ exhibits a monoclinic $C2/m$ distortion due to collinear JT-elongated octahedra, which disappears on heating during a first-order transition which onsets at 460 K[23−27] (see Figure 1) to the aristotype $R\bar{3}m$ structure. $LiMnO_2$ and $NaMnO_2$ exhibit polymorphism and more complex cooperative ordering.[13] $LiNiO_2$ is a complicated case, with clear experimental evidence for multiple Ni−O bond lengths[28−30] but diffraction data are typically modeled with the

https://doi.org/10.1021/jacs.4c09922
J. Am. Chem. Soc. 2024, 146, 29560−29574

aristotype structure which does not allow for cooperative JT ordering. There have been a broad array of proposed forms of JT ordering[30,31] for $LiNiO_2$, with the energetically most-favorable being a zigzag ordering with monoclinic $P2_1/c$ symmetry.[17,31−34] Alternative phenomena for $LiNiO_2$ involving spin- or even charge-disproportionation,[32,34,35] have also been proposed; these are likely a feature of other nickelates such as $AgNiO_2$[36,37] or the nickelate perovskites.[38−40] In contrast to a recent theoretical study,[13] which concludes that the layered alkali metal transition metal oxides ABO_2 (A=Li, Na; B=Ni, Mn) should exhibit an order−disorder JT transition, we have recently found evidence for a displacive transition in $LiNiO_2$ using *ab initio* Molecular Dynamics (AIMD) and variable-temperature X-ray diffraction (XRD).[17]

In this work, we have studied the variable-temperature properties of $NaNiO_2$. We use variable-temperature synchrotron X-ray diffraction, neutron total scattering, Ni K edge extended X-ray absorption fine structure (EXAFS), ^{23}Na magic-angle spinning (MAS) solid state nuclear magnetic resonance (NMR) spectroscopy, and AIMD to study the changes in $NaNiO_2$ with a focus on the local Ni environment through the monoclinic→ rhombohedral transition at ∼460 K where the cooperative JT distortion disappears. We find evidence of a displacive JT transition, in contrast to the majority of previous studies on Jahn−Teller transitions which report order−disorder transitions. Taken together with previous results,[17,27] this suggests a broader conclusion that the JT transitions in layered triangular-lattice nickelates are different from those in the transition metal perovskites where local JT distortions are reported to persist in the high-temperature phase.

2. RESULTS

2.1. Variable-Temperature Synchrotron X-ray Diffraction. Variable-temperature synchrotron X-ray powder diffraction was performed to observe temperature-dependent changes in the average crystal structure and analyzed by Rietveld refinement.[41] On heating, the crystal structure of $NaNiO_2$ is monoclinic ($C2/m$) until ∼460 K where Bragg peaks associated with the high-temperature rhombohedral ($R\bar{3}m$) phase begin to emerge, indicating this is approximately the onset of the cooperative transition temperature T_{JT}. A mixed-phase regime exists, in which the phase fraction of the monoclinic phase decreases with heating, until the sample becomes entirely rhombohedral around 505 K. These findings are consistent with previous variable-temperature diffraction studies of $NaNiO_2$.[24−26]

Selected results of the Rietveld analysis are shown in Figure 2, with further information in Section S2. The volume per formula unit is larger in the rhombohedral than the monoclinic structure (Figure 2b). There is positive thermal expansion in both the monoclinic and rhombohedral phases. In the monoclinic phase, the NiO_6 octahedral volume is essentially temperature-independent [inset of Figure 2b] and the volume increase is entirely driven by NaO_6 octahedral expansion. Through the phase transition, there is a discontinuous increase in unit cell volume per formula unit, primarily due to a ∼1.2% jump in NiO_6 octahedral volume (compared with a ∼0.6% increase for NaO_6 octahedra) from the fully monoclinic to fully rhombohedral phases. In the rhombohedral phase both the NiO_6 and NaO_6 octahedra expand on heating at around the same rate.

Figure 2c shows that there is a significant increase in interlayer distance on heating from the monoclinic to rhombohedral structures. Figure 2d shows that the two different intralayer distances (corresponding to Ni−Ni and Na−Na distances within the plane of the layer) of the monoclinic cell equalize in the rhombohedral cell, due to the increase in cell symmetry, and the distance in the rhombohedral cell is slightly decreased compared with the average distance in the monoclinic cell.

2.2. ^{23}Na Nuclear Magnetic Resonance. A variable-temperature ^{23}Na NMR (VT-NMR) experiment was carried out to investigate changes in the local structure with temperature using both magic angle spinning (MAS) and static measurements. Changes in both of the spectra are observed at T_{JT} (Figure S37). At low temperatures a single Na^+ environment is observed consistent with the average structure of monoclinic $NaNiO_2$. A second higher chemical shift environment is observed on heating which we ascribe to Na^+ in the high-temperature, rhombohedral phase of $NaNiO_2$. There is a limited T-range where both peaks coexist until at higher T only a single peak persists. Both environments have large hyperfine shifts due to the presence of paramagnetic Ni^{3+} ions, the peak shifting to lower values as the Ni^{3+} become less paramagnetic at higher temperatures. These results are consistent with the diffraction data and indicate a change in the local Na^+ environment at T_{JT}.

2.3. Neutron Pair Distribution Function. Total scattering neutron experiments have been performed on $NaNiO_2$. The Bragg data was published previously[27] and is consistent with the synchrotron XRD presented in the previous section.

Pair Distribution Functions (PDFs), presented as $D(r)$ in Figure 3a,[42] were obtained from the neutron total scattering data at 293 and 450 K (both monoclinic average structure), and 500 K (rhombohedral average structure). There are two Ni−O peaks at 293 and 450 K, consistent with the Ni−O bond length splitting due to a Jahn−Teller distortion, and a single Ni−O peak at 500 K, implying that NiO_6 octahedra are undistorted by

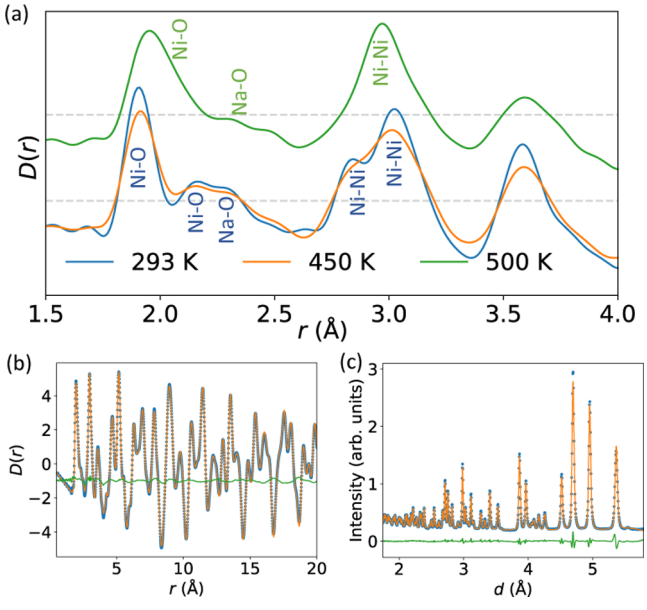

Figure 3. (a) Experimental neutron PDFs for $NaNiO_2$ at 293, 450, and 500 K, in the r-range where the nearest-neighbor Ni−O peaks occur. Peaks are labeled for the 293 K data set in blue text and 500 K data set in green text. The 500 K data is vertically offset from the low-temperature data for ease of distinguishing the changes compared with the lower-T data sets. Gray dashed horizontal lines occur at $D(r)$ = 0 for the lower two temperatures (lower) and 500 K (upper). (b,c) Example fits to the PDF and Bragg diffraction data at 500 K using the supercell fitting (experimental data: blue; fitted data: orange; difference pattern; green).

https://doi.org/10.1021/jacs.4c09922
J. Am. Chem. Soc. 2024, 146, 29560−29574

the Jahn−Teller effect at this temperature. This is consistent with the picture from the average structure, as described from the variable-temperature synchrotron data. However, at 500 K the Ni−O peak is highly asymmetric with a tail on the high-r side.

Initial analysis of the PDF data was performed using small-box analysis, also known as real-space Rietveld refinement. Results are presented in Section S3.1. The room-temperature data can be fit well with the JT-distorted, monoclinic structure used for Rietveld analysis of the reciprocal space data. The PDF data at 500 K can be fit adequately with both the monoclinic and the rhombohedral (JT-undistorted) structures, with a slightly higher R_{wp} for the rhombohedral structure (although this is to be expected given the smaller number of free parameters). In the monoclinic cell, the difference between the Ni−O bond lengths is very small at 500 K (∼0.041 Å, compared with ∼0.243 Å at 293 K), which is not consistent with the presence of a local Jahn−Teller distortion.

Ultimately the small-box analysis did not fit all features of the PDF data, and in any case small-box analysis with a single unit cell would be insensitive to some types of local Jahn−Teller ordering. To test for the presence of local Jahn−Teller distortions obscured by the peak asymmetry, big-box analysis was performed on the PDF data, in conjunction with the Bragg scattering data.

To this end, a rhombohedral $NaNiO_2$ unit cell with centered orthorhombic setting was prepared, consisting of 6 formula units and obtained via transformation from the normal rhombohedral cell using eq S5. A $16 \times 9 \times 3$ supercell of this unit cell was used as the starting point for big box refinements, with lattice dimensions ∼45 Å and containing 10 368 atoms; see Methods for further details. The atomic positions in this model were then refined against the experimental data. Here, empirical bond valence sum[43] restraints (discussed in Methods) were applied to the atomic positions to ensure physical behavior, although qualitatively equivalent results are obtained without these restraints [Section S3.9]. The big box refinements were run several times to ensure reproducibility [Section S3.11].

An example fit at 500 K to both the reciprocal-space and real-space data sets can be seen in Figure 3b,c and the resulting supercells are shown in Figure 4. Qualitatively, it can be seen by simple inspection of the O−Ni−O layers in the supercell that there is a cooperative Q_3 (Figure S1) elongation of the NiO_6 octahedra at 293 K (the Jahn−Teller distortion) which does not seem to be present at 500 K. These supercells are quantitatively analyzed in terms of the Ni−O bond length distribution (Figure 5a) and it can be seen that below the monoclinic→ rhombohedral transition there are two clusters of Ni−O bond lengths: a shorter cluster representing four bonds and a longer cluster with two bonds. However, at 500 K there is just a single cluster, which is not consistent with Jahn−Teller-distorted octahedra. The model is consistent with the significant peak asymmetry in the Ni−O bond length observed in the PDF data, with the peak asymmetry occurring as a consequence of the broader bond length distribution for longer bonds.

Other evidence for the absence of Jahn−Teller distortion in the local structure of rhombohedral $NaNiO_2$ can be obtained by considering two metrics for the octahedral distortion. The bond length distortion index (BLDI),[44] Figure 5b, quantifies the deviation of bond lengths from the average for a given polyhedron and is often used to quantify Jahn−Teller distortions.[27,46,47] For a big box model where thermal effects are modeled by deviation of atoms from their average positions

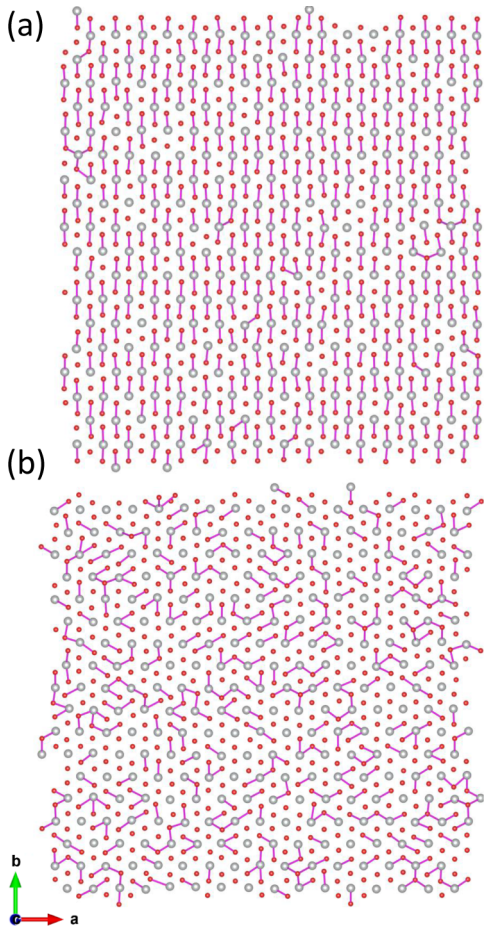

Figure 4. Cross sections of the *ab* plane for a single O−Ni−O layer of the supercell obtained by big box PDF analysis, showing the distribution of elongated (r > 2.1 Å) Ni−O bonds at (a) 293 K and (b) 500 K. Na ions are hidden for clarity. Ni: gray; O: red.

(rather than using atomic displacement parameters, as is conventional for Rietveld refinement), we would expect the BLDI to increase with heating in the absence of any electronic or magnetostructural transitions. The average BLDI for all NiO_6 octahedra is 0.0547 and 0.0575 (to 3 significant figures) at 293 and 450 K, respectively, in the monoclinic phase, before decreasing to 0.0458 at 500 K. This is clearly shown by the decreasing distribution of bond lengths in Figure 5a. In contrast, the average BLDI continuously increases with heating for the NaO_6 octahedra, increasing from 0.0260 at 293 K, to 0.0352 at 450 K, and finally 0.0450 at 500 K (see Figure S10). This trend in the BLDI for NiO_6 octahedra can be explained by the disappearance of a local Jahn−Teller distortion at T_{JT}. We can also quantify the distortion using the parameter ρ_0, where $\rho_0^2 = Q_2^2 + Q_3^2$. Figure 5c shows $P(\rho_0)$, the probability of octahedra having a given value of ρ_0, defined as

$$P(\rho_0) = \frac{f(\rho_0)}{2\pi\rho_0} \quad (1)$$

where $f(\rho_0)$ is a histogram of ρ_0 for all NiO_6 octahedra. This parametrization shows maximum probability at $\rho_0 \approx 0$ at 500 K, compared with large nonzero magnitudes at 293 and 450 K, which also indicates the absence of a local Jahn−Teller distortion in the rhombohedral phase. This result that the most probable ρ_0 substantially decreases at 500 K, compared

https://doi.org/10.1021/jacs.4c09922
J. Am. Chem. Soc. 2024, 146, 29560−29574

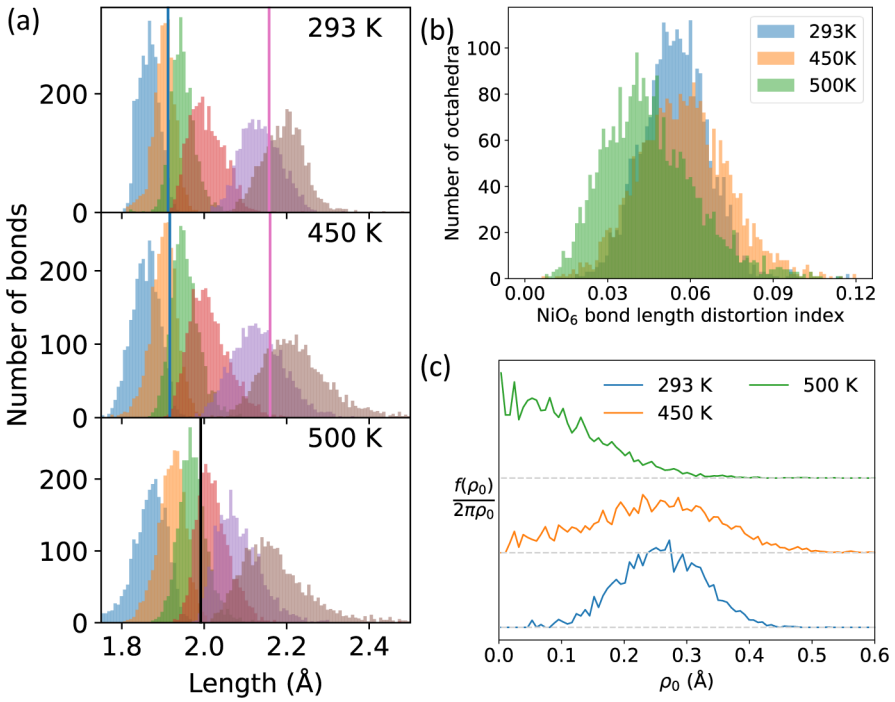

Figure 5. (a) Ni−O bond distributions at 293 K (top), 450 K (middle), and 500 K (bottom), as obtained via big box analysis of neutron PDF data, for the smallest to largest Ni−O bond in each octahedron; vertical lines are the bond lengths from Rietveld refinement of the neutron data reported in ref 27. (b) Histogram of bond length distortion index[44] for each NiO_6 octahedron at 293, 450, and 500 K. (c) Probability function of distortion (eq 1) at 293, 450, and 500 K. (b) and (c) are obtained using VanVleckCalculator.[6,45]

with lower temperatures, is resilient to other ways of running the big box refinement, for instance with different starting configurations [Section S3.7], changes in the BVS restraints [Section S3.9], and multiple runs with the same starting parameters [Section S3.11].

2.4. X-ray Absorption Spectroscopy. XAS at the Ni K edge was performed, with analysis focusing on the extended X-ray absorption fine structure (EXAFS) in real-space. These data, $\chi(r)$, are similar to a partial PDF of Ni−O bond lengths, but with the significant difference that there is a phase shift resulting in peaks in $\chi(r)$ being down-shifted by around 0.5 Å. It is therefore a useful supplement to the PDF data. The room-temperature $\chi(r)$ data presented here resembles the EXAFS on $NaNiO_2$ reported previously.[48]

Both the X-ray absorption near edge structure (XANES) and EXAFS change on heating through T_{JT} (Figure 6). In the XANES, although there is no change in peak position (indicating that the Ni oxidation state does not change from Ni^{3+}) there is a pre-edge feature around 8335 eV in $d\mu/dE$ which is more prominent for the $T < T_{JT}$ regime than the $T > T_{JT}$ regime. This pre-edge is likely due to quadrupole forbidden transitions, and will be less prominent in higher symmetry Ni environments. This observation is therefore consistent with the absence of a local Jahn−Teller distortion at $T > T_{JT}$.

The EXAFS data, Figure 6b, also show a significant change on heating. The two peaks corresponding to two Ni−Ni interatomic distances at ∼2.5 Å when $T < T_{JT}$ merge into a single peak in the $T > T_{JT}$ regime, consistent with the single Ni−Ni interatomic distance in the rhombohedral structure. The peak at ∼1.5 Å corresponds to the Ni−O bond, which exhibits a far more subtle change in shape through the Jahn−Teller transition than the Ni−Ni peak, and fitting to the data is required to examine the changes in local structure.

Models were obtained using FEFF[49] and refined against the $\chi(r)$ data over different ranges. Two ranges were considered: one with just the Ni−O shell r = 0.5−2.0 Å, and the other r = 0.5−3.1 Å to also include the Ni−Ni interatomic distances. Models with both 1 or 2 Ni−O and Ni−Ni distances were considered and we describe these using curly braces enclosing the comma-separated values for the number of lengths for each bond; for instance a model with a single Ni−O distance in the reduced range is described as {1,0}, whereas a model with two Ni−O bond lengths and two Ni−Ni bond lengths is described as {2,2}. Five models were used, over both ranges: {1,0}, {2,0}, {1,1}, {2,1}, and {2,2}. Models in which the first number is 1 correspond to JT-undistorted, and models where the first number is 2 are compatible with a JT distortion.

The data in the Ni−O range (0.5 Å to 2.0 Å) were fitted well with both the JT-distorted {2,0} and JT-undistorted {1,0} models (Figure S32) at all studied temperatures, with the {2,0} model consistently fitting better than the {1,0} model. It is then necessary to determine whether the improved fit is due to a more realistic model or simply due to the additional number of refined parameters with the JT-distorted {2,0} model. We consider two figures of merit for evaluating fitting quality, the reduced χ^2 ($r\chi^2$) and the Bayesian Information Criterion (BIC).[50] The T-dependence of these parameters, Figure 6(d), indicates that, in the monoclinic regime, model {2,0} better describes the data (consistent with the established picture of static cooperative JT-distorted NiO_6 octahedra), but when $T > T_{JT}$ the model {2,0} only achieves a better fit as it has more refined parameters; i.e., the JT-undistorted model {1,0} is the better description of the Ni−O shell. In addition, for $T > T_{JT}$ the short and long Ni−O bond lengths converge within error for the {2,0} model (Figure S33).

Over the larger range (0.5 Å to 3.1 Å) fitting was performed using models {2,2}, {2,1}, and {1,1}. When $T < T_{JT}$, the {1,1}

https://doi.org/10.1021/jacs.4c09922
J. Am. Chem. Soc. 2024, 146, 29560−29574

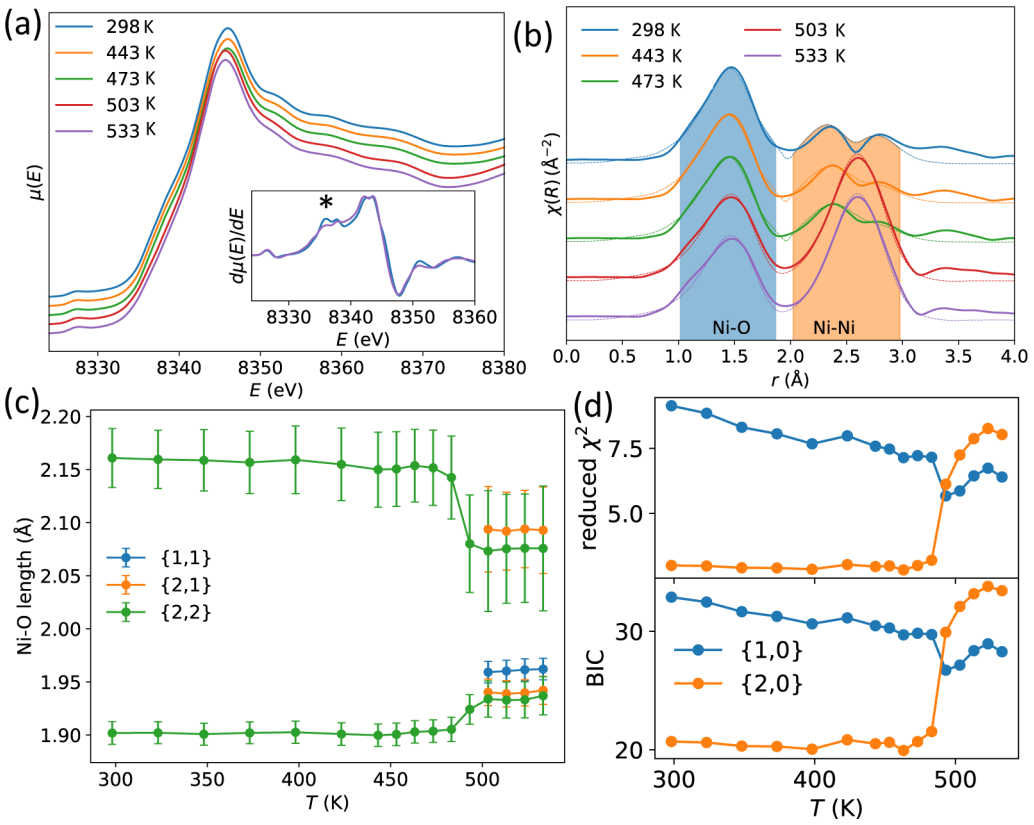

Figure 6. (a) XANES at the Ni K edge at various temperatures, where each spectrum is offset by an arbitrary amount for clarity; inset shows dμ/dE for the 298.15 and 533.15 K, with an asterisk marking the feature on the rising edge. (b) EXAFS data at the Ni K edge, with heating, for $NaNiO_2$ at various temperatures, with the solid line representing the fit with a {2,2} model consisting of two Ni−O bond lengths and two Ni−Ni interatomic distances. The feature around 3.4 Å is the Ni−Na atomic distance, which was not included in any of the fitting. (c) Short and long Ni−O bond lengths obtained from fitting the {2,2} and {2,1} models to the EXAFS data; Ni−O lengths from fitting the {1,1} model are also shown. (d) Figures of merit for fits performed with the {2,0} and {1,0} models, reduced χ^2 and Bayesian Information Criteria (BIC), in the vicinity of the Ni−O bond only.

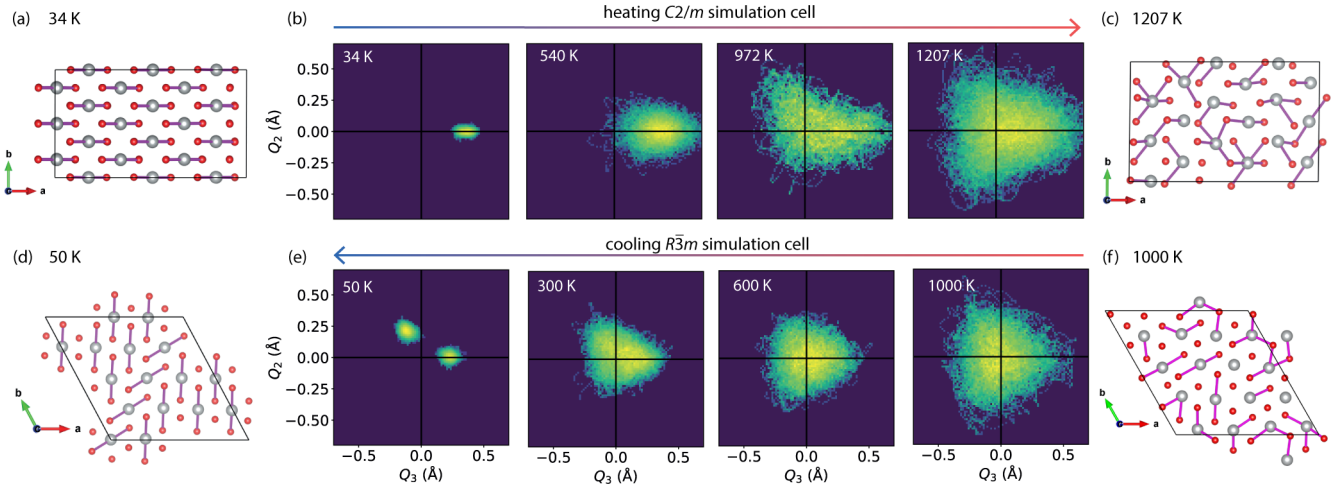

Figure 7. (a,c,d,f) Snapshots of a NiO_6 layer as obtained from AIMD simulations with $C2/m$ (a,c) and $R\bar{3}m$ (d,f) starting configurations, at various temperatures. Ni: gray; O: red. Ni−O bonds above 2.1 Å are shown. (b,e) Van Vleck $E_g(Q_2, Q_3)$ diagrams as a function of temperature for both configurations, showing the displacive transition; note that a rotation of 120° from the $Q_2 = 0$ line means a change in the axis of elongation. Analogous figures based on the PDF big box analysis can be seen in Figure S11.

and {2,1} models perform poorly as they cannot reproduce the Ni−Ni splitting observed experimentally, Figure 6b. The temperature-dependence of the figures of merit, Figure S30, indicate that below T_{JT}, {2,2} is the favored model, consistent with diffraction. Above T_{JT}, all three models qualitatively fit the data well, but the two figures of merit support different models; BIC favors the undistorted model {1,1} whereas $r\chi^2$ the {2,2} model.

Does the EXAFS data support the possibility of a local Jahn−Teller distortion in $NaNiO_2$ above T_{JT}? This seems unlikely for the following reasons. First, when the fit is restricted solely to the Ni−O bonds the JT-undistorted model {1,0} fits best according

https://doi.org/10.1021/jacs.4c09922
J. Am. Chem. Soc. 2024, 146, 29560−29574

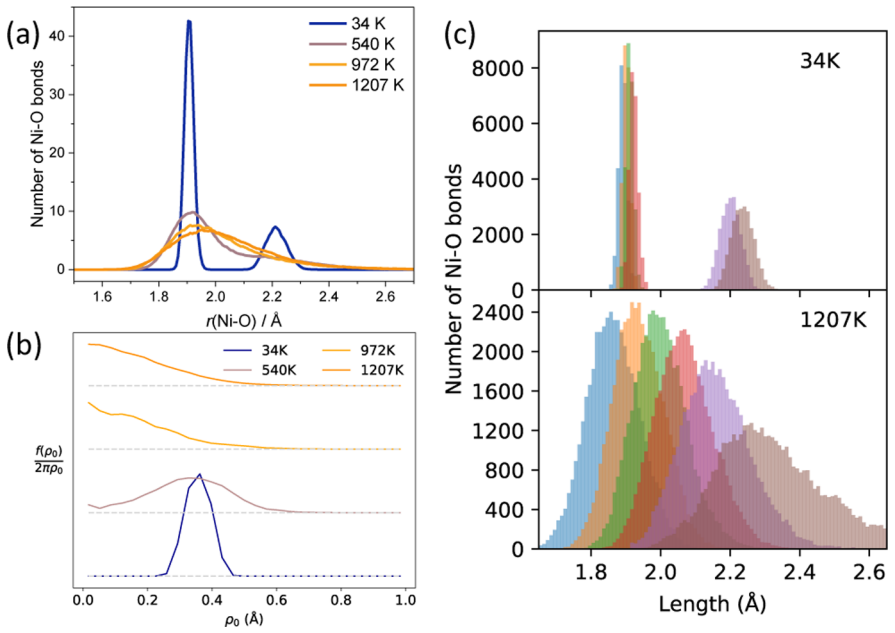

Figure 8. (a) Calculated Ni−O pair distribution functions from AIMD; these are convolved with experimental Q_{max} in Figure S36. (b) The probability function of ρ_0 [eq 1] from AIMD, for the cells with the $C2/m$ starting structure. (c) Ni−O bond lengths at two temperatures for AIMD runs from the $C2/m$ starting structure.

to both metrics. Second, the Ni−O bond length separation for the {2,2} model (~0.15 Å, Figure 6c) is significantly reduced compared to the separation at $T < T_{JT}$ (around 0.27 Å), which differs from the order−disorder transition in $LaMnO_3$ where there is little change in bond length from EXAFS.[15] Third, when we plot histograms of the four shortest and two longest Ni−O bonds in the big box PDF data at 500 K, Figure S10, which is analogous to the {2,···} models used for the EXAFS fitting, we also observe a bond length separation despite other forms of analysis showing the absence of Jahn−Teller distortions according to the PDF data; this suggests that the {2,2} EXAFS model is consistent with a thermally disordered, JT-undistorted state above T_{JT}. For these reasons, even if the {2,2} model is favored by EXAFS above T_{JT}, this could be explained without requiring a local Jahn−Teller distortion. We therefore interpret the EXAFS data as consistent with the absence of local Jahn−Teller distortions for $T > T_{JT}$.

2.5. *Ab Initio* Molecular Dynamics. *Ab initio* molecular dynamics simulations of $NaNiO_2$ simulation cells starting with a collinear ordering of Jahn−Teller distortions, in a 3 × 3 × 3 supercell (216 ions) expanded from the monoclinic cell, were performed at temperatures between 34 and 1207 K (Figure 7a,c). Both the cell shape and volume were allowed to change. At low temperatures, the AIMD trajectories show thermal vibrations but the JT distortions persist, and remain collinear. On heating, the distortions decrease in magnitude and are no longer aligned to a single axis. At high temperatures, the octahedra approach a JT-undistorted state.

The temperature-dependence of the Jahn−Teller distortions is quantified by looking at the Ni−O PDF (Figure 8a) and the probability function of ρ_0 (Figure 8b). At low temperatures (34 K), the PDF shows distinct peaks corresponding to short and long Ni−O bonds with a large, positive ρ_0. On heating (972 K, 1207 K) the two peaks in the PDF merge to a single broad asymmetric peak. ρ_0 significantly decreases, with the highest probability at $\rho_0 = 0$. This can also be seen in the heat map distributions in $E_g(Q_2, Q_3)$ shown in Figure 7.

However, at these high temperatures there remains a residual distortion evident from a small asymmetry in the Ni−O PDF distribution, with a preference for elongation along the collinear axis (Figure 7b 1207 K). We attribute this to the finite simulation cell size enforcing a periodicity in the structure that may cause longer-range correlations of the NiO_6 octahedra. To explore this, simulations were run from a similarly sized starting configuration (4 × 4 × 1 expansion of the rhombohedral unit cell; 192 ions) without JT distortions, and hence without interoctahedral correlations to begin with, cooling the sample from 1000 K. The same underlying behavior is observed as seen in the simulations starting from JT distorted simulation cells, i.e., distortions are observed at $T < T_{JT}$ that vanish at $T > T_{JT}$ and (re)emerge at $T < T_{JT}$. At ca. 1000 K, the NiO_6 octahedra are fully isotropic (Figure 7e 1000 K). On cooling, Jahn−Teller distortions emerge. These are row-ordered (Figure 7e 300 K), i.e., arranged collinearly within a row, rather than across the simulation cell, as predicted previously.[33] The rows show a preference for two out of the three possible directions of the distortions (i.e., arctan $(Q_2/Q_3) = 0$ or $2\pi/3$ but never $4\pi/3$), resulting in two clusters of data points in the van Vleck plot at low temperatures (Figure 7e 50 K). This is likely a consequence of the very small domain sizes, resulting presumably from the rapid cooling on the time scale of the AIMD simulations (a few picoseconds), not allowing the system to arrange into a macroscopically collinear ground state. We note that in the transition regime for both simulation cells, the octahedral distortions are elongated along two out of the three octahedral axes (Figure 7b 972 K,(e) 300 K), suggesting the transitions between the collinearly distorted phase with elongations along one axis and the displacive phase with random fluctuations along all axes may occur through an intermediate state with distortions occurring preferentially along two axes. If cooled slowly, the distortions are expected to order collinearly, whereas the rapid quenching of the AIMD simulation freezes in the distortions.

The calculated transition temperature between the JT-distorted state and the JT-undistorted state depends on the

https://doi.org/10.1021/jacs.4c09922
J. Am. Chem. Soc. 2024, 146, 29560−29574

initial configuration of the simulation cell, and this does not change when the length of the AIMD runs is extended further. On heating the distorted simulation cell, the onset of the JT-transition T_{onset} is found to occur at around 586 K, i.e., at a slightly higher temperature than the experimental onset temperature obtained from synchrotron X-ray diffraction, 460 K. On cooling the undistorted simulation cell, the onset of the transition T_{onset} is below 300 K, i.e., slightly lower than the experimental onset temperature. A closer look at these differences in T_{onset} reveals that there are two factors causing the deviations. First, as the transition is a first-order transition, hysteric behavior is expected, i.e., the transition temperature is expected to differ between heating and cooling, and, albeit to a smaller extent, hysteresis has been observed experimentally, too.[25,26] Second, the AIMD simulations starting from the distorted and undistorted simulation cells result in different domain sizes, affecting the transition temperatures further. The cooperative collinear distortions of the distorted simulation cell correspond to a scenario of infinitely large domains which shift the transition temperature to its maximum value. When cooling the undistorted simulation cell, very small domains form (Figure 7e 300 K) resulting in short-range correlations between octahedral distortions. The transition temperature obtained from cooling the undistorted simulation cell therefore constitutes a lower cutoff to the transition temperature from the JT-undistorted phase to the distorted phase. The AIMD simulations thus predict the transition from the JT-distorted to the JT-undistorted phase to occur at $T < 586$ K, and the transition from the JT-undistorted to the JT-distorted phase at temperatures $T > 300$ K. The onset temperature derived for the transition to the JT-undistorted phase based on synchrotron XRD of samples of intermediate domain sizes in this study, 460 K, lies approximately in the middle of the predicted temperature window.

3. DISCUSSION

Our studies of the local Ni^{3+} environment, using neutron PDF and Ni K edge EXAFS, suggest the absence of local static Jahn–Teller-distortions for $T > T_{JT}$. Further, while a dynamic Jahn–Teller distortion[4] has previously been suggested for $LiNiO_2$,[51−53] by analogy with similar proposals for $LaMnO_3$,[54] such a dynamic Jahn–Teller distortion would also be resolvable via our neutron PDF and EXAFS measurements. These observations suggest that the JT transition in $NaNiO_2$ is better characterized as displacive rather than order–disorder.[13] This is different to the observations of an order–disorder transition in $LaMnO_3$,[14,15,18,19] and the proposed order–disorder transition for $NaNiO_2$.[13] To our knowledge, only in $LiNiO_2$[17] has prior evidence for a displacive Jahn–Teller transition been put forward, using AIMD and inferences from changes in strain.

As in previous reports we observe a first order phase transition in $NaNiO_2$ with the monoclinic and rhombohedral phases coexisting over a finite temperature range. The observed discontinuous increase in unit cell volume from the monoclinic to the rhombohedral structures (Figure 2) is also consistent with a first-order phase transition. The positive thermal expansion through the transition is consistent, via the Clausius–Clapeyron equation, with our previous finding[27] of $dT_{JT}/dp > 0$. We note that in the displacive transition in $SrTiO_3$[55] a positive dT_c/dp is also observed. In contrast, a negative thermal expansion is found at the transition temperature in $LaMnO_3$[56] and ferroelectric $PbTiO_3$,[57,58] both order–disorder transitions, with $dT_c/dp < 0$.[59,60] The displacive transition may therefore be related to the sign of dT_{JT}/dp.

In $NaNiO_2$, the high-temperature phase will be enthalpically unfavorable and hence the phase transition will be entropically driven, according to the free energy $\Delta G = \Delta H - T\,\Delta S$, where ΔH is the enthalpy change, T is temperature, and ΔS is the entropy change. There are two relevant contributions to the entropy: configurational and vibrational. We find the configurational entropy of orbital disorder for $LiNiO_2$ and $NaNiO_2$ to be subextensive (see Appendix A), meaning it does not increase with increasing system size.[61] A subextensive configurational entropy has also been found for an Ising model on an elastic triangular lattice.[62] Consequently the entropy term is dominated by dynamic vibrational effects which disfavor local Jahn–Teller distortions. This is likely a contributing factor in the displacive JT transition we have observed, and is in contrast to high-temperature $LaMnO_3$ where, by analytic and Monte Carlo calculations using the Potts model, there is extensive configurational entropy of orbital disorder[20,21] and hence an order–disorder transition.

An alternative hypothesis we considered for the disappearance of Jahn–Teller distortions in high-temperature $NaNiO_2$ was the possibility for delocalization of the electrons resulting in a change in the energy landscape of the system. This is by analogy to the insulator-to-metal transition (IMT) previously observed in the perovskite nickelates.[63,64] However, while variable-temperature conductivity, $\sigma(T)$, data from ref 65 [Figure S6], shows an increase in conductivity by several orders of magnitude on heating, there is no change of sign of $d\sigma(T)/dT$. This is similar to the conductivity data for $LaMnO_3$,[54] which would suggest the electronic conductivity is not closely related to the order–disorder/displacive nature of the transition.

There are a number of other differences between $NaNiO_2$ and $LaMnO_3$ which could affect the Jahn–Teller transition. For instance, the edge-sharing octahedral connectivity in $NaNiO_2$ results in much larger intraoctahedral angular distortion compared with the corner-sharing octahedra in $LaMnO_3$. This difference in connectivity is a consequence of the triangular Ni network in $NaNiO_2$. Given the constraint that axes of elongation of adjacent JT-distorted Ni atoms cannot point at the same O anion, there are no possible long-range JT-disordered configurations,[30] which means that this triangular Ni network cannot host a Potts-type Jahn–Teller disorder such as that proposed for $LaMnO_3$.[16,20,21] Another difference is that d^4 Mn^{3+} is generally found to be JT-distorted, whereas nominally d^7 Ni^{3+} is susceptible to other types of electronic configuration such as charge disproportionation;[36−40] this may be due to the smaller electronegativity difference between Ni–O, compared with Mn–O, which has been argued to cause charge-transfer insulating[66] behavior in many nickelates.[64,67,68] Attempting to deconvolute the role of these different factors will require further study on the transition in other Jahn–Teller-distorted materials, along with theoretical and computational work.

Whether or not a JT transition is displacive or order–disorder may be important in some battery cathode materials. This will be particularly apparent if the JT transition occurs below room-temperature, as it does in, for instance, the $NaNi_xCo_{1-x}O_2$ solid solution for $x \leq 0.8$[65] and the spinel $LiMn_2O_4$.[69] In these cases, the presence or absence of local JT distortions will result in different ionic mobility, and will impact the crystallographic changes that occur with electrochemical cycling. The implications of this on electrochemistry should be studied in future works.

https://doi.org/10.1021/jacs.4c09922
J. Am. Chem. Soc. 2024, 146, 29560−29574

4. CONCLUSION

We have shown that the Jahn−Teller transition in $NaNiO_2$ is displacive in character, with the absence of local JT-distortions or orbital ordering in the NiO_6 octahedra at $T > T_{JT}$ (T_{JT} being the cooperative Jahn−Teller transition temperature). To our knowledge this is the first time that local probes of structure have shown a displacive Jahn−Teller transition, though order−disorder transitions have been reported for other JT-distorted materials such as perovskite $LaMnO_3$.[14,15,18,19] Our findings are not consistent with previous computational studies on $NaNiO_2$, which predicted an order−disorder transition with persisting local JT distortions,[13] but our own *ab initio* molecular dynamics calculations support our experimental findings. This complementarity between local probe experiments and simulation provides further support for our earlier *ab initio* molecular dynamics study on $LiNiO_2$ which also predicted a displacive JT transition.[17]

We found that the configurational entropy of orbital disorder is subextensive in layered transition metal oxides such as $NaNiO_2$, and contrast this to the extensive configurational entropy[20] in the case of perovskites such as $LaMnO_3$. Further theoretical work is required to better understand these different behaviors.

5. METHODS

5.1. Sample Synthesis. Samples were prepared by solid state synthesis. Na_2O_2 (Alfa Aesar; 95%) and NiO (Alfa Aesar; 99.995%) were mixed and pelletized in a 1.05:1 molar ratio of Na:Ni, with excess Na to account for Na-loss during heating. The pelletized precursor mixture was placed in an alumina crucible and heated to 973 K for 70 h in a tube furnace under a constant flow of O_2. O_2 was maintained throughout the heating and cooling processes. The sample showed a color change from light green (the NiO/Na_2O_2 precursor mixture) to black, indicating successful synthesis. To prevent reaction with moisture, the sample was stored and handled in an inert Ar-atmosphere. The same sample was previously studied in ref 27, where electron microscopy and Rietveld[41] analysis of laboratory X-ray diffraction and neutron diffraction data were presented.

5.2. Synchrotron X-ray Diffraction. Variable-temperature, ambient-pressure synchrotron X-ray diffraction was performed using the I11 instrument[70,71] at Diamond Light Source (λ = 0.824110 Å) using the Mythen-2 position-sensitive detector, with a data collection time of ∼10 s. The sample was contained in a 0.5 mm diameter glass capillary, sealed inside a glovebox with epoxy (Loctite Double Bubble). The sample was heated at a rate of 12 K/min from 322 to 796 K, with periodic measurements.

Data were analyzed by sequential Rietveld refinement[41] using the software package Topas 7.[72] A pseudo-Voigt peak function was used, and background was fitted using a Chebyshev polynomial with 20 terms. A small correction for preferred orientation was applied, using the March-Dollase model.[73,74]

5.3. Nuclear Magnetic Resonance. Samples for variable-temperature nuclear magnetic resonance (VT-NMR) were packed into 4 mm ZrO_2 magic angle spinning (MAS) rotors in an Ar filled glovebox, and fitted with ZrO_2 caps. ^{23}Na chemical shifts were calibrated using solid NaCl as an external secondary reference (7.21 ppm relative to 1 M NaCl(aq) at 0.0 ppm). ^{23}Na MAS NMR spectra were acquired using a Bruker Avance IIIHD spectrometer ($\nu_0[^1H]$ = 500.13 MHz, $\nu_0[^{23}Na]$ = 132.46 MHz, $\nu_0[^{207}Pb]$ = 104.26 MHz), with a Bruker 4 mm HX probe and 14 kHz MAS. Projection magic-angle turning and a phase-adjusted sideband separation (pj-MATPASS) pulse sequence was used to obtain the isotropic ^{23}Na spectra.[75]

Static VT-NMR samples were measured in the same spectrometer using a Bruker HX static probe. A Hahn-echo pulse sequence with $\pi/4$ = 2.05 μs optimized on solid $NaNiO_2$ was used. Temperature was calibrated through a NMR shift thermometer compound $Pb(NO_3)_2$, based on the known temperature-dependence of the isotropic chemical shift of $Pb(NO_3)_2$.[76] ^{207}Pb NMR spectra were acquired with the same probe at the same temperature values, using a Hahn-echo pulse sequence. The isotropic chemical shift values for $Pb(NO_3)_2$ were obtained by fitting the data using the SOLA fitting program within Topspin 4.1.4.

5.4. Neutron Total Scattering. Variable-temperature total-scattering neutron diffraction was performed on the NOMAD instrument[77] at the Spallation Neutron Source, Oak Ridge National Laboratory, USA. $NaNiO_2$ was stored under Ar in a sealed NMR tube (2 cm sample height, 5 mm outer diameter) for the measurements. Heating was performed using a furnace, at a rate of 5 K/min. The sample was measured on heating at 293 K, 450 K, 500 K, and after cooling at 316 K. The neutron diffraction data and the refined crystal structure were previously published in ref 27. In the Fourier transform to real space, a sliding Q_{max} as a function of r is used, with Q_{max} = 40 Å^{-1} at low-r and gradually decreasing Q_{max} beyond that, with Q_{max} = 20 Å^{-1} above r = 25 Å.

5.5. Analysis of Pair Distribution Function. Small-box pair distribution function analysis, also known as real-space Rietveld refinement, was performed using Topas 6.[72] Data were fitted in the range 1.0 Å to 10 Å in real space only. The starting structures were the normal $C2/m$ and $R\bar{3}m$ structures used commonly in the literature for the low- and high-temperature phases of $NaNiO_2$.

Pair distribution function analysis was performed via a "big box" approach used Topas 7,[72] following a modified version of the method introduced in ref 78. A supercell model was refined against both the Bragg data from NOMAD bank 4 (as defined in ref 77) and the experimental neutron pair distribution function. In this refinement, atomic coordinates were refined until convergence following the Rietveld algorithm.[41] During initial iterations, restraints were applied to prevent large atomic movements, but these were removed in later stages of the refinement. Upon convergence, each atom was randomly shifted by a distance less than or equal to 0.1% of the unit cell size (∼0.045 Å) in each spatial dimension to help minimization. This typically occurred several hundred times. The final configuration was the converged structure with the best fit quality. Our approach differs from the more commonly-used approach in RMCProfile.[79] Data were fitted in the range 0.5 Å to 20 Å in real space.

A 16 × 9 × 3 supercell of a pseudo-orthorhombic cell (space group: $P1$; $a \approx 2.846$ Å; $b \approx 5.321$ Å; $c \approx 15.703$ Å; $\beta = \gamma = 90°$; α = 90° for the 500 K supercell and ∼88° for the $T < T_{JT}$ supercells) was used for the refinements. This $NaNiO_2$ unit cell was obtained via transformation from the rhombohedral cell using eq S5. The supercell has edge lengths ∼45 Å and contains 10 368 atoms. In this analysis, the thermal parameters for all atoms were fixed at low values (B_{iso} = 0.01 Å^2) such that thermal effects are modeled by the deviation of each site from its ideal position. To ensure that chemically reasonable models were obtained, soft restraints were included. The relative weighting of restraints against data was set to ensure refinements were not

https://doi.org/10.1021/jacs.4c09922
J. Am. Chem. Soc. 2024, 146, 29560−29574

dominated by restraints. The Supporting Information includes refinements performed in the absence of restraints to check their influence on the conclusions drawn (Section S3.9). The main soft restraint was the calculated bond valence sum[43] (as an analog for oxidation state), V_{calc}, of cations deviates from its expected value (Na: +1; Ni: +3), an established approach[80] in PDF analysis.[78,81−103] Here, V_{calc} is calculated as follows:

$$V_{calc} = \sum_{i=1}^{6} \exp\left[\frac{r_0 - r_i}{B}\right] \quad (2)$$

where the empirical parameters r_0 and B are based on the cation and anion species, and r_i are the bond lengths between the metal atom and the ith oxygen. In this work, B = 0.37 Å, r_0^{Na} = 1.672 Å and r_0^{Ni} = 1.7335 Å; these values were selected to give average bond lengths of 2.335 and 1.99 Å for NaO_6 and NiO_6 octahedra, respectively, to match the room-temperature average structure.

Since the $P1$ space group has a floating origin, a restraint was applied to keep the average shift of Ni sites close to zero.

The supercells obtained from refinement were then analyzed using VanVleckCalculator,[6,45] a Python 3[104] code which is based on PyMatGen.[105]

5.6. Ni K Edge X-ray Absorption Spectroscopy. X-ray absorption spectroscopy (XAS) measurements were performed on the BM23 instrument[106] of the European Synchrotron Radiation Facility (ESRF), France. Powdered $NaNiO_2$ was mixed homogeneously with a powdered boron nitride binder (~16 mg: ~ 70 mg $NaNiO_2$:BN) and pressed into a 13 mm pellet in a dry, oxygen-free nitrogen environment. The pellet was cut and placed in a sealed sample holder under flowing helium. Temperature control was achieved using a resistive heater, and at each temperature the sample was left for 6 min to thermally equilibriate. At each temperature the sample was measured ten times to ensure reproducibility, and an average spectrum produced. X-ray absorption was measured in the vicinity of the Ni K edge (~8.3 keV).

X-ray absorption was calculated using the Beer−Lambert law[107] comparing X-ray intensity in ionization chambers before and after transmission through the sample, and a third ionization chamber measured the absorption through Ni foil as a reference. Data normalization was performed using the Python-based[104] Larch[108] package. For the normalization of the data, a pre-edge range between −350 eV and −45 eV from the edge center was fit with a straight line, and the postedge region between 200 and 1250 eV was fit with a quadratic polynomial. Data were transformed from E-space to k-space via the transform $k = \sqrt{\frac{2m_e}{\hbar^2}(\hbar\omega - E_0)}$, where m_e is the mass of the electron, E_0 is the edge energy, and ω is the frequency of the measured photon. Finally, the EXAFS function $\chi(k)$ was obtained by fitting and subtracting a spline to the EXAFS data in k-space, where R_{bkg} was set to 1 Å and the spline was fit within a k-range of 0 $Å^{-1}$ to 18.25 $Å^{-1}$, with a k^2-weighting. For the Fourier transform of EXAFS from k-space to r-space, a k-range of 2.5 $Å^{-1}$ to 15 $Å^{-1}$ was used, and to minimize Fourier ripples from the cutoffs in k-space, a Kaiser-Bessel window with end width dk = 7 $Å^{-1}$ was applied to the data in k-space before the transformation.

Calculated EXAFS data were obtained by multiple-scattering path expansion using FEFF,[49] as implemented in Larch in Python. In this model, data are fit using the EXAFS equation over each set of equivalent paths j, defined as follows:

$$\chi(k) = S_0^2 \sum_j \frac{N_j \left|f_j(k)\right|}{kR_j^2} \sin[2kR_j + \phi_j(k)] \times \exp\left[-\frac{2R_j}{\lambda_j(k)}\right] \exp(-\sigma_j^2 k^2) \quad (3)$$

where FEFF is used to calculate scattering amplitude $|f_j(k)|$, photoelectron mean free path $\lambda_j(k)$, and phase $\varphi_j(k)$ for all paths. N_j is the number of equivalent paths for each j, which is fixed. The amplitude reduction factor S_0^2 was kept fixed at a value obtained by fitting against the Ni foil reference, S_0^2 = 0.79286024. The path distance R_j and Debye−Waller factors σ_j for each path were refined during model fitting. The edge position E_0 was also freely refined.

5.7. *Ab Initio* Molecular Dynamics. AIMD simulations were performed according to the Generalized Gradient Approximation (GGA)[109] and the projector augmented wave method (PAW),[110] as implemented in the Vienna Ab Initio Simulation Package (VASP).[111,112] The plane-wave energy cutoff was set to 500 eV. Supercells are expansions of the monoclinic (3 × 3 × 3; 216 ions) and rhombohedral (4 × 4 × 1; 192 ions) unit cells, respectively. Simulations were performed at the Γ point and checked against calculations with a 2×2×2 Monkhorst−Pack[113] k-point grid for consistency. The convergence criteria for the electronic and ionic relaxations were set to 10^{-6} eV and 5 × 10^{-3} eV/Å, respectively.

For Ni, the $4s^2 3d^8$ electrons were treated as valence electrons. To account for the strongly correlated d electrons, a rotationally invariant Hubbard U parameter[114] of U_{eff} = 6 eV was selected, which was used successfully in previous studies of layered oxide cathodes, both for 0 K DFT calculations and finite temperature AIMD simulations.[17,115,116] For oxygen, the $2s^2 2p^4$ electrons were considered as valence electrons.

AIMD simulations were performed for the isothermal−isobaric ensemble (NpT, constant pressure, particle number, and temperature) at zero pressure, allowing the cell shape and volume to change. A Langevin thermostat was used with friction coefficients set to zero to minimize impact on the lattice vibrations. Trajectories were run for 3 ps at timesteps of 1 fs. Following an equilibration period of 1 ps, snapshots were sampled every 2−5 fs, using Ovito[117], for the analysis of the distortions.

APPENDIX A

Proof of subextensive configurational entropy for orbital disorder

Here, a mathematical proof is presented that, given a set of assumptions, there is subextensive configurational entropy of orbital disorder in layered oxide materials based on a triangular array of JT-active cations. We define subextensive as meaning that the configurational entropy does not increase with increasing system size.

This relies on three basic axioms:

(1) The effect on orbital ordering of interlayer interactions is negligible.
(2) Each oxygen anion participates in precisely one Jahn−Teller-elongated bond.
(3) Jahn−Teller distortions are purely of the Q_3 tetragonal elongation type.

Axiom (1) is justified because the O−A−O (A=Li,Na) layers prevent orbital interactions because the Na does not overly constrain the position of the O atom and there is not much

https://doi.org/10.1021/jacs.4c09922
J. Am. Chem. Soc. 2024, 146, 29560−29574

correlation between the O atoms around an Na site. Axiom (2) because participation in more than one JT-elongated bond would make the O anion under-bonded. Axiom (3) because this is how octahedra are at room-temperature in $NaMO_2$ (M=Ni,Mn) materials.

Configurational entropy per layer is given by

$$S_{\text{config}}^{\text{layer}} = \ln[W_{\text{layer}}] \tag{A.1}$$

where W_{layer} is the number of configurations within the layer. Note we define entropy in units of Boltzmann's constant k_B. Given Axiom 2, there are only two possible alignments of the elongated axes between neighboring octahedra. Either the axes of elongation are parallel ("A") or angled 120° apart ("B"). There are three rows of Ni sites within a layer, separated by an angle of 120°. In a monoclinic cell such as that of $NaNiO_2$ at $T < T_{JT}$, all interactions would be of the "A" type. If there were true orbital disorder, each chain would be a random combination of these two possible configurations "A" and "B", for instance "AABBABAAABAABBABABB". If L is the length of such a chain (divided by Ni−Ni distance), then we have the following number of configurations:

$$W_{\text{layer}} = 3 \times 2^{L} = 3 \times 2^{A^{1/2}} \tag{A.2}$$

where the factor of three arises because there are three directions along which chains occur, and we relate L to an arbitrary area A via $L = A^{1/2}$. Given that N is proportional to A, where N is the number of Jahn−Teller-elongated axes within an area of the single layer, we can use $N = \alpha A$ and substitute this into the equation for configurational entropy as follows:

$$S_{\text{config}}^{\text{layer}} = \ln[3 \times 2^{\alpha' N^{1/2}}] = C + N^{1/2}\ln[2] \tag{A.3}$$

where we have used $\alpha' = \alpha^{1/2}$ and used constant $C = \ln[3] + \alpha'\ln[2]$. If we then calculate configurational entropy per NiO_6 octahedron for a large system, as $N \to \infty$, $C/N \to 0$ and so:

$$\frac{S_{\text{config}}^{\text{layer}}}{N} \approx N^{-1/2}\ln[2]. \tag{A.4}$$

Therefore, as $N \to \infty$, so does $\frac{S_{\text{config}}^{\text{layer}}}{N} \to 0$. This indicates that the configurational entropy of orbital disorder is subextensive.

■ ASSOCIATED CONTENT

Data Availability Statement

Data from the BM23 instrument at the European Synchrotron Radiation Facility are available at doi:10.15151/ESRF-ES-962076745.[118] All other data is available in the University of Cambridge repository at doi.org/10.17863/CAM.112349.[119]

Supporting Information

The Supporting Information is available free of charge at https://pubs.acs.org/doi/10.1021/jacs.4c09922.

A description of the Van Vleck modes. Further analysis of supercell outputs of big box PDF analysis, and results from various different starting configurations. Expanded AIMD results. NMR data. Tabulated results of all analysis techniques (PDF)

■ AUTHOR INFORMATION

Corresponding Authors

Liam A. V. Nagle-Cocco − *Cavendish Laboratory, University of Cambridge, Cambridge CB3 0HE, United Kingdom;* orcid.org/0000-0001-9265-1588; Email: lavn2@cam.ac.uk

Siân E. Dutton − *Cavendish Laboratory, University of Cambridge, Cambridge CB3 0HE, United Kingdom;* orcid.org/0000-0003-0984-5504; Email: sed33@cam.ac.uk

Authors

Annalena R. Genreith-Schriever − *Yusuf Hamied Department of Chemistry, University of Cambridge, Cambridge CB2 1EW, United Kingdom;* orcid.org/0000-0001-5626-2438

James M. A. Steele − *Cavendish Laboratory, University of Cambridge, Cambridge CB3 0HE, United Kingdom; Yusuf Hamied Department of Chemistry, University of Cambridge, Cambridge CB2 1EW, United Kingdom;* orcid.org/0000-0002-1075-3634

Camilla Tacconis − *Cavendish Laboratory, University of Cambridge, Cambridge CB3 0HE, United Kingdom;* orcid.org/0000-0003-1128-1023

Joshua D. Bocarsly − *Cavendish Laboratory, University of Cambridge, Cambridge CB3 0HE, United Kingdom; Yusuf Hamied Department of Chemistry, University of Cambridge, Cambridge CB2 1EW, United Kingdom;* Present Address: Department of Chemistry, University of Houston, Houston, Texas 77 204−5003, United States of America; orcid.org/0000-0002-7523-152X

Olivier Mathon − *European Synchrotron Radiation Facility, Grenoble 38043, France*

Joerg C. Neuefeind − *Spallation Neutron Source, Oak Ridge National Laboratory, Oak Ridge, Tennessee 37831, United States of America*

Jue Liu − *Spallation Neutron Source, Oak Ridge National Laboratory, Oak Ridge, Tennessee 37831, United States of America;* orcid.org/0000-0002-4453-910X

Christopher A. O'Keefe − *Yusuf Hamied Department of Chemistry, University of Cambridge, Cambridge CB2 1EW, United Kingdom;* orcid.org/0000-0003-3115-0768

Andrew L. Goodwin − *Inorganic Chemistry Laboratory, Department of Chemistry, University of Oxford, Oxford OX1 3QR, United Kingdom;* orcid.org/0000-0001-9231-3749

Clare P. Grey − *Yusuf Hamied Department of Chemistry, University of Cambridge, Cambridge CB2 1EW, United Kingdom;* orcid.org/0000-0001-5572-192X

John S. O. Evans − *Department of Chemistry, Durham University, Durham DH1 3LE, United Kingdom;* orcid.org/0000-0001-6305-6341

Complete contact information is available at: https://pubs.acs.org/10.1021/jacs.4c09922

Funding

This work was supported by the Faraday Institution (FIRG001, FIRG017, FIRG024, FIRG060). L.A.V.N−C acknowledges a scholarship EP/R513180/1 to pursue doctoral research from the UK Engineering and Physical Sciences Research Council (EPSRC) and additional funding from the Cambridge Philosophical Society. J.M.A.S. acknowledges support from the EPSRC Cambridge NanoCDT, EP/L015978/1. A.L.G. acknowledges European Research Council (ERC) funding under grant 788144.

Notes

The authors declare no competing financial interest.

■ ACKNOWLEDGMENTS

The authors acknowledge Oak Ridge National Laboratory, a United States Department of Energy Office of Science User Facility, for use of the NOMAD instrument at the Spallation Neutron Source (experiment IPTS25164). We acknowledge the European Synchrotron Radiation Facility for provision of beam time on BM23 (experiment CH6437). We acknowledge I11 beamline at the Diamond Light Source, UK, for the synchrotron XRD measurement done under BAG proposal (the data presented in this work under CY34243; essential preliminary data from CY28349). Calculations were performed using the Sulis Tier 2 HPC platform hosted by the Scientific Computing Research Technology Platform at the University of Warwick (EP/T022108/1). We would like to thank Dr Euan N. Bassey, Lucy Haddad, Dr Anastasia Yu. Molokova, Dr Chloe C. Coates, Dr Farheen N. Sayed, Dr Gheorghe-Lucian Păşcuţ, and Dr João Elias F. S. Rodrigues for useful discussions. Crystal structure figures were prepared using VESTA-3[120] and plots were prepared using MatPlotLib.[121]

■ REFERENCES

(1) Jahn, H. A.; Teller, E. Stability of polyatomic molecules in degenerate electronic states-I—Orbital degeneracy. *Proc. R. Soc. London, Ser. A* **1937**, *161*, 220–235.
(2) Öpik, U.; Pryce, M. H. L. Studies of the Jahn–Teller effect. I. A survey of the static problem. *Proc. R. Soc. London, Ser. A* **1957**, *238*, 425–447.
(3) Longuet-Higgins, H. C.; Öpik, U.; Pryce, M. H. L.; Sack, R. A. Studies of the Jahn–Teller effect. II. The dynamical problem. *Proc. R. Soc. London, Ser. A* **1958**, *244*, 1–16.
(4) Goodenough, J. B. Jahn–Teller phenomena in solids. *Annu. Rev. Mater. Sci.* **1998**, *28*, 1–27.
(5) Van Vleck, J. H. The Jahn–Teller Effect and Crystalline Stark Splitting for Clusters of the Form XY_6. *J. Chem. Phys.* **1939**, *7*, 72–84.
(6) Nagle-Cocco, L. A. V.; Dutton, S. E. Van Vleck Analysis of Angularly Distorted Octahedra using VanVleckCalculator. *IUCr J. Appl. Crystallogr.* **2024**, *57*, 20–33.
(7) Fil, D. V.; Tokar, O. I.; Shelankov, A. L.; Weber, W. Lattice-mediated interaction of Cu^{2+} Jahn–Teller ions in insulating cuprates. *Phys. Rev. B* **1992**, *45*, 5633.
(8) Keller, H.; Bussmann-Holder, A.; Müller, K. A. Jahn–Teller physics and high-T_c superconductivity. *Mater. Today* **2008**, *11*, 38–46.
(9) Khomskii, D. I.; Streltsov, S. V. Orbital effects in solids: Basics, recent progress, and opportunities. *Chem. Rev.* **2021**, *121*, 2992–3030.
(10) Kim, H.; Yoon, G.; Park, I.; Park, K.-Y.; Lee, B.; Kim, J.; Park, Y.-U.; Jung, S.-K.; Lim, H.-D.; Ahn, D.; et al. Anomalous Jahn–Teller behavior in a manganese-based mixed-phosphate cathode for sodium ion batteries. *Energy Environ. Sci.* **2015**, *8*, 3325–3335.
(11) Li, X.; Wang, Y.; Wu, D.; Liu, L.; Bo, S.-H.; Ceder, G. Jahn–Teller assisted Na diffusion for high performance Na ion batteries. *Chem. Mater.* **2016**, *28*, 6575–6583.
(12) Choi, J. U.; Kim, J.; Hwang, J.-Y.; Jo, J. H.; Sun, Y.-K.; Myung, S.-T. $K_{0.54}[Co_{0.5}Mn_{0.5}]O_2$New cathode with high power capability for potassium-ion batteries. *Nano Energy* **2019**, *61*, 284–294.
(13) Radin, M. D.; Thomas, J. C.; Van der Ven, A. Order-disorder versus displacive transitions in Jahn–Teller active layered materials. *Phys. Rev. Mater.* **2020**, *4*, 043601.
(14) Qiu, X.; Proffen, T.; Mitchell, J. F.; Billinge, S. J. L. Orbital correlations in the pseudocubic *O* and rhombohedral *R* phases of $LaMnO_3$. *Phys. Rev. Lett.* **2005**, *94*, 177203.
(15) Souza, R. A.; Ramos, A. Y.; Tolentino, H. C. N.; Granado, E. Local structure in $LaMnO_3$ across the Jahn–Teller transition. *Phys. Scr.* **2005**, *2005*, 428.
(16) Thygesen, P. M. M.; Young, C. A.; Beake, E. O. R.; Romero, F. D.; Connor, L. D.; Proffen, T. E.; Phillips, A. E.; Tucker, M. G.; Hayward, M. A.; Keen, D. A.; Goodwin, A. L. Local structure study of the orbital order/disorder transition in $LaMnO_3$. *Phys. Rev. B* **2017**, *95*, 174107.
(17) Genreith-Schriever, A. R.; Alexiu, A.; Phillips, G. S.; Coates, C. S.; Nagle-Cocco, L. A. V.; Bocarsly, J. D.; Sayed, F. N.; Dutton, S. E.; Grey, C. P. Jahn–Teller distortions and phase transitions in $LiNiO_2$: Insights from *ab initio* molecular dynamics and variable-temperature X-ray diffraction. *Chem. Mater.* **2024**, *36*, 2289–2303.
(18) Araya-Rodriguez, E.; Ramos, A. Y.; Tolentino, H. C. N.; Granado, E.; Oseroff, S. B. Local distortion in $LaMnO_3$ across the Jahn–Teller transition. *J. Magn. Magn. Mater.* **2001**, *233*, 88–90.
(19) García, J.; Subías, G.; Sánchez, M.; Blasco, J. Jahn–Teller Dynamic Distortions in $LaMnO_3$ Determined by EXAFS. *Phys. Scr.* **2005**, *2005*, 594.
(20) Ahmed, M. R.; Gehring, G. A. The phase diagram of an anisotropic Potts model. *J. Phys. A: Math. Gen.* **2005**, *38*, 4047.
(21) Ahmed, M. R.; Gehring, G. A. Potts model for the distortion transition in $LaMnO_3$. *Phys. Rev. B* **2006**, *74*, 014420.
(22) Ahmed, M. R.; Gehring, G. A. Volume collapse in $LaMnO_3$ studied using an anisotropic Potts model. *Phys. Rev. B* **2009**, *79*, 174106.
(23) Dyer, L. D.; Borie Jr, B. S.; Smith, G. P. Alkali metal-nickel oxides of the type $MNiO_2$. *J. Am. Chem. Soc.* **1954**, *76*, 1499–1503.
(24) Dick, S.; Müller, M.; Preissinger, F.; Zeiske, T. The structure of monoclinic $NaNiO_2$ as determined by powder X-ray and neutron scattering. *Powder Diffr.* **1997**, *12*, 239–241.
(25) Chappel, E.; Nunez-Regueiro, M. D.; Chouteau, G.; Isnard, O.; Darie, C. Study of the ferrodistorsive orbital ordering in $NaNiO_2$ by neutron diffraction and submillimeter wave ESR. *Eur. Phys. J. B* **2000**, *17*, 615–622.
(26) Sofin, M.; Jansen, M. New route of preparation and properties of $NaNiO_2$. *Z. Naturforsch. B* **2005**, *60*, 701–704.
(27) Nagle-Cocco, L. A. V.; Bull, C. L.; Ridley, C. J.; Dutton, S. E. Pressure Tuning the Jahn–Teller Transition Temperature in $NaNiO_2$. *Inorg. Chem.* **2022**, *61*, 4312–4321.
(28) Pickering, I. J.; George, G. N.; Lewandowski, J. T.; Jacobson, A. J. Nickel K-edge X-ray absorption fine structure of lithium nickel oxides. *J. Am. Chem. Soc.* **1993**, *115*, 4137–4144.
(29) Rougier, A.; Delmas, C.; Chadwick, A. V. Non-cooperative Jahn–Teller effect in $LiNiO_2$: An EXAFS study. *Solid State Commun.* **1995**, *94*, 123–127.
(30) Chung, J.-H.; Proffen, T.; Shamoto, S.; Ghorayeb, A. M.; Croguennec, L.; Tian, W.; Sales, B. C.; Jin, R.; Mandrus, D.; Egami, T. Local structure of $LiNiO_2$ studied by neutron diffraction. *Phys. Rev. B* **2005**, *71*, 064410.
(31) Chen, Z.; Zou, H.; Zhu, X.; Zou, J.; Cao, J. First-principle investigation of Jahn–Teller distortion and topological analysis of chemical bonds in $LiNiO_2$. *J. Solid State Chem.* **2011**, *184*, 1784–1790.
(32) Chen, H.; Freeman, C. L.; Harding, J. H. Charge disproportionation and Jahn–Teller distortion in $LiNiO_2$ and $NaNiO_2$: A density functional theory study. *Phys. Rev. B* **2011**, *84*, 085108.
(33) Radin, M. D.; Van der Ven, A. Simulating charge, spin, and orbital ordering: Application to Jahn–Teller distortions in layered transition-metal oxides. *Chem. Mater.* **2018**, *30*, 607–618.
(34) Foyevtsova, K.; Elfimov, I.; Rottler, J.; Sawatzky, G. A. $LiNiO_2$ as a high-entropy charge-and bond-disproportionated glass. *Phys. Rev. B* **2019**, *100*, 165104.
(35) Poletayev, A. D.; Green, R. J.; Swallow, J. E. N.; An, L.; Jones, L.; Harris, G.; Bencok, P.; Sutaro, R.; Cottom, J. P.; Morgan, B. J.; House, R. A.; Weatherup, R. S.; Islam, M. S. *Temperature-Dependent Dynamic Disproportionation in $LiNiO_2$*, arXiv, 2024.
(36) Wawrzyńska, E.; Coldea, R.; Wheeler, E. M.; Mazin, I. I.; Johannes, M. D.; Sörgel, T.; Jansen, M.; Ibberson, R. M.; Radaelli, P. G. Orbital degeneracy removed by charge order in triangular antiferromagnet $AgNiO_2$. *Phys. Rev. Lett.* **2007**, *99*, 157204.
(37) Kang, J.-S.; Lee, S. S.; Kim, G.; Lee, H. J.; Song, H. K.; Shin, Y. J.; Han, S. W.; Hwang, C.; Jung, M. C.; Shin, H. J.; Kim, B. H.; Kwon, S. K.; Min, B. I. Valence and spin states in delafossite $AgNiO_2$ and the

https://doi.org/10.1021/jacs.4c09922
J. Am. Chem. Soc. 2024, 146, 29560–29574

frustrated Jahn−Teller system $ANiO_2$ (A = Li, Na). *Phys. Rev. B* **2007**, *76*, 195122.
(38) García-Muñoz, J.; Rodríguez-Carvajal, J.; Lacorre, P. Neutron-diffraction study of the magnetic ordering in the insulating regime of the perovskites $RNiO_3$ (R = Pr and Nd). *Phys. Rev. B* **1994**, *50*, 978.
(39) Mizokawa, T.; Khomskii, D. I.; Sawatzky, G. A. Spin and charge ordering in self-doped Mott insulators. *Phys. Rev. B* **2000**, *61*, 11263.
(40) Garcia-Munoz, J. L.; Aranda, M. A. G.; Alonso, J. A.; Martinez-Lope, M. J. Structure and charge order in the antiferromagnetic band-insulating phase of $NdNiO_3$. *Phys. Rev. B* **2009**, *79*, 134432.
(41) Rietveld, H. M. A profile refinement method for nuclear and magnetic structures. *J. Appl. Crystallogr.* **1969**, *2*, 65−71.
(42) Keen, D. A. A comparison of various commonly used correlation functions for describing total scattering. *J. Appl. Crystallogr.* **2001**, *34*, 172−177.
(43) Brown, I. D.; Altermatt, D. Bond-valence parameters obtained from a systematic analysis of the inorganic crystal structure database. *Acta Crystallogr. Sect. B: Struct. Sci.* **1985**, *41*, 244−247.
(44) Baur, W. H. The geometry of polyhedral distortions. Predictive relationships for the phosphate group. *Acta Crystallogr., Sect. B: Struct. Crystallogr. Cryst. Chem.* **1974**, *30*, 1195−1215.
(45) Nagle-Cocco, L. A. V. *GitHub*. https://github.com/lnaglecocco/VanVleckCalculator. (Accessed 20 August 2024).
(46) Kimber, S. A. J. Charge and orbital order in frustrated $Pb_3Mn_7O_{15}$. *J. Phys.: Condens. Matter* **2012**, *24*, 186002.
(47) Lawler, K. V.; Smith, D.; Evans, S. R.; Dos Santos, A. M.; Molaison, J. J.; Bos, J.-W. G.; Mutka, H.; Henry, P. F.; Argyriou, D. N.; Salamat, A.; Kimber, S. A. J. Decoupling Lattice and Magnetic Instabilities in Frustrated $CuMnO_2$. *Inorg. Chem.* **2021**, *60*, 6004−6015.
(48) Jacquet, Q.; Mozhzhukhina, N.; Gillespie, P. N. O.; Wittmann, G.; Ramirez, L. P.; Capone, F. G.; Rueff, J.-P.; Belin, S.; Dedryvère, R.; Stievano, L.; Matic, A. A Fundamental Correlative Spectroscopic Study on $Li_{1-x}NiO_2$ and $NaNiO_2$. *Adv. Energy Mater.* **2024**, 2401413.
(49) Newville, M. EXAFS analysis using FEFF and FEFFIT. *J. Synchrotron Radiat.* **2001**, *8*, 96−100.
(50) Neath, A. A.; Cavanaugh, J. E. The Bayesian information criterion: Background, derivation, and applications. *Wiley Interdiscip. Rev.: Comput. Stat.* **2012**, *4*, 199−203.
(51) Stoyanova, R.; Zhecheva, E.; Friebel, C. Magnetic interactions in layered $LiNiO_2$ revealed by EPR of Ni^{3+}. *J. Phys. Chem. Solids* **1993**, *54*, 9−13.
(52) Sugiyama, J.; Ikedo, Y.; Mukai, K.; Nozaki, H.; Månsson, M.; Ofer, O.; Harada, M.; Kamazawa, K.; Miyake, Y.; Brewer, J. H.; Ansaldo, E. J.; Chow, K. H.; Watanabe, I.; Ohzuku, T. Low-temperature magnetic properties and high-temperature diffusive behavior of $LiNiO_2$ investigated by muon-spin spectroscopy. *Phys. Rev. B* **2010**, *82*, 224412.
(53) Sicolo, S.; Mock, M.; Bianchini, M.; Albe, K. And yet it moves: $LiNiO_2$, a dynamic Jahn−Teller system. *Chem. Mater.* **2020**, *32*, 10096−10103.
(54) Zhou, J.-S.; Goodenough, J. B. Paramagnetic phase in single-crystal $LaMnO_3$. *Phys. Rev. B* **1999**, *60*, R15002.
(55) Fossheim, K.; Berre, B. Ultrasonic Propagation, Stress Effects, and Interaction Parameters at the Displacive Transition in $SrTiO_3$. *Phys. Rev. B* **1972**, *5*, 3292.
(56) Chatterji, T.; Fauth, F.; Ouladdiaf, B.; Mandal, P.; Ghosh, B. Volume collapse in $LaMnO_3$ caused by an orbital order-disorder transition. *Phys. Rev. B* **2003**, *68*, 052406.
(57) Rossetti, G. A.; Cline, J. P.; Navrotsky, A. Phase transition energetics and thermodynamic properties of ferroelectric $PbTiO_3$. *J. Mater. Res.* **1998**, *13*, 3197−3206.
(58) Pan, Z.; Fang, Y.-W.; Nishikubo, T.; Hu, L.; Kawaguchi, S.; Azuma, M. Tolerance factor control of tetragonality and negative thermal expansion in $PbTiO_3$-based ferroelectrics. *Chem. Mater.* **2022**, *34*, 2798−2803.
(59) Zhou, J.-S.; Uwatoko, Y.; Matsubayashi, K.; Goodenough, J. B. Breakdown of magnetic order in Mott insulators with frustrated superexchange interaction. *Phys. Rev. B* **2008**, *78*, 220402.
(60) Sani, A.; Hanfland, M.; Levy, D. Pressure and Temperature Dependence of the Ferroelectric−Paraelectric Phase Transition in $PbTiO_3$. *J. Solid State Chem.* **2002**, *167*, 446−452.
(61) Camp, P. J.; Fuertes, A.; Attfield, J. P. Subextensive entropies and open order in perovskite oxynitrides. *J. Am. Chem. Soc.* **2012**, *134*, 6762−6766.
(62) Shokef, Y.; Souslov, A.; Lubensky, T. C. Order by disorder in the antiferromagnetic Ising model on an elastic triangular lattice. *Proc. Natl. Acad. Sci. U. S. A.* **2011**, *108*, 11804−11809.
(63) Alonso, J. A.; García-Muñoz, J. L.; Fernández-Díaz, M. T.; Aranda, M. A. G.; Martínez-Lope, M. J.; Casais, M. T. Charge disproportionation in $RNiO_3$ perovskites: Simultaneous metal-insulator and structural transition in $YNiO_3$. *Phys. Rev. Lett.* **1999**, *82*, 3871.
(64) Bisogni, V.; Catalano, S.; Green, R. J.; Gibert, M.; Scherwitzl, R.; Huang, Y.; Strocov, V. N.; Zubko, P.; Balandeh, S.; Triscone, J.-M.; et al. Ground-state oxygen holes and the metal−insulator transition in the negative charge-transfer rare-earth nickelates. *Nat. Commun.* **2016**, *7*, 1−8.
(65) Delmas, C.; Saadoune, I.; Dordor, P. Effect of cobalt substitution on the Jahn−Teller distortion of the $NaNiO_2$ layered oxide. *Mol. Cryst. Liq. Cryst. Sci. Technol., Sect. A* **1994**, *244*, 337−342.
(66) Zaanen, J.; Sawatzky, G. A.; Allen, J. W. Band gaps and electronic structure of transition-metal compounds. *Phys. Rev. Lett.* **1985**, *55*, 418.
(67) Ronda, C.; Arends, G. J.; Haas, C. Photoconductivity of the nickel dihalides and the nature of the energy gap. *Phys. Rev. B* **1987**, *35*, 4038.
(68) Foyevtsova, K.; Sawatzky, G. A. A Band Theory Perspective on Molecular Orbitals in Complex Oxides. *J. Mod. Phys.* **2019**, *10*, 953.
(69) Yamada, A.; Tanaka, M. Jahn−Teller structural phase transition around 280 K in $LiMn_2O_4$. *Mater. Res. Bull.* **1995**, *30*, 715−721.
(70) Thompson, S. P.; Parker, J. E.; Potter, J.; Hill, T. P.; Birt, A.; Cobb, T. M.; Yuan, F.; Tang, C. C. Beamline I11 at Diamond: A new instrument for high resolution powder diffraction. *Rev. Sci. Instrum.* **2009**, *80* (7), 075107.
(71) Thompson, S. P.; Parker, J. E.; Marchal, J.; Potter, J.; Birt, A.; Yuan, F.; Fearn, R. D.; Lennie, A. R.; Street, S. R.; Tang, C. C. Fast X-ray powder diffraction on I11 at Diamond. *J. Synchrotron Radiat.* **2011**, *18*, 637−648.
(72) Coelho, A. A. TOPAS and TOPAS-Academic: An optimization program integrating computer algebra and crystallographic objects written in C++. *J. Appl. Crystallogr.* **2018**, *51*, 210−218.
(73) March, A. Mathematische Theorie der Regelung nach der Korngestalt bei affiner Deformation. *Z. Krist. -Cryst. Mater.* **1932**, *81*, 285−297.
(74) Dollase, W. A. Correction of intensities for preferred orientation in powder diffractometry: Application of the March model. *J. Appl. Crystallogr.* **1986**, *19*, 267−272.
(75) Hung, I.; Zhou, L.; Pourpoint, F.; Grey, C. P.; Gan, Z. Isotropic high field NMR spectra of Li-ion battery materials with anisotropy > 1 MHz. *J. Am. Chem. Soc.* **2012**, *134*, 1898−1901.
(76) Takahashi, T.; Kawashima, H.; Sugisawa, H.; Baba, T. ^{207}Pb chemical shift thermometer at high temperature for magic angle spinning experiments. *Solid State Nucl. Magn. Reson.* **1999**, *15*, 119−123.
(77) Neuefeind, J.; Feygenson, M.; Carruth, J.; Hoffmann, R.; Chipley, K. K. The nanoscale ordered materials diffractometer NOMAD at the spallation neutron source SNS. *Nucl. Instrum. Methods Phys. Res., Sect. B* **2012**, *287*, 68−75.
(78) Fuller, C. A.; Berrod, Q.; Frick, B.; Johnson, M. R.; Avdeev, M.; Evans, J. S. O.; Evans, I. R. Oxide ion and proton conductivity in highly oxygen-deficient cubic perovskite $SrSc_{0.3}Zn_{0.2}Ga_{0.5}O_{2.4}$. *Chem. Mater.* **2020**, *32*, 4347−4357.
(79) Tucker, M. G.; Keen, D. A.; Dove, M. T.; Goodwin, A. L.; Hui, Q. RMCProfile: Reverse Monte Carlo for polycrystalline materials. *J. Phys.: Condens. Matter* **2007**, *19*, 335218.
(80) Norberg, S. T.; Tucker, M. G.; Hull, S. Bond valence sum: A new soft chemical constraint for RMCProfile. *J. Appl. Crystallogr.* **2009**, *42*, 179−184.

(81) Marrocchelli, D.; Madden, P. A.; Norberg, S. T.; Hull, S. Cation composition effects on oxide conductivity in the $Zr_2Y_2O_7$-Y_3NbO_7 system. *J. Phys.: Condens. Matter* **2009**, *21*, 405403.
(82) Abrahams, I.; Liu, X.; Hull, S.; Norberg, S. T.; Krok, F.; Kozanecka-Szmigiel, A.; Islam, M. S.; Stokes, S. J. A combined total scattering and simulation approach to analyzing defect structure in Bi_3YO_6. *Chem. Mater.* **2010**, *22*, 4435−4445.
(83) Liu, X.; Abrahams, I.; Hull, S.; Norberg, S. T.; Holdynski, M.; Krok, F. A neutron total scattering study of defect structure in $Bi_3Nb_{0.5}Y_{0.5}O_{6.5}$. *Solid State Ionics* **2011**, *192*, 176−180.
(84) Norberg, S. T.; Eriksson, S. G.; Hull, S. Comparison of short-range ion−ion correlations in the α, β and δ phases of Bi_2O_3. *Solid State Ionics* **2011**, *192*, 409−412.
(85) Norberg, S. T.; Hull, S.; Ahmed, I.; Eriksson, S. G.; Marrocchelli, D.; Madden, P. A.; Li, P.; Irvine, J. T. S. Structural Disorder in Doped Zirconias, Part I: The $Zr_{0.8}Sc_{0.2-x}Y_xO_{1.9}$ ($0.0 \leq x \leq 0.2$) System. *Chem. Mater.* **2011**, *23*, 1356−1364.
(86) Norberg, S. T.; Thomas, P. A.; Tucker, M. G. A neutron total scattering study of local coordination in $KTiOPO_4$ from room temperature to 900°C. *J. Phys.: Condens. Matter* **2011**, *23*, 175401.
(87) Burbano, M.; Norberg, S. T.; Hull, S.; Eriksson, S. G.; Marrocchelli, D.; Madden, P. A.; Watson, G. W. Oxygen vacancy ordering and the conductivity maximum in Y_2O_3-doped CeO_2. *Chem. Mater.* **2012**, *24*, 222−229.
(88) Chong, S. Y.; Szczecinski, R. J.; Bridges, C. A.; Tucker, M. G.; Claridge, J. B.; Rosseinsky, M. J. Local structure of a pure Bi A site polar perovskite revealed by pair distribution function analysis and reverse Monte Carlo modeling: Correlated off-Axis displacements in a rhombohedral material. *J. Am. Chem. Soc.* **2012**, *134*, 5836−5849.
(89) Norberg, S. T.; Hull, S.; Eriksson, S. G.; Ahmed, I.; Kinyanjui, F.; Biendicho, J. J. Pyrochlore to fluorite transition: The $Y_2(Ti_{1-x}Zr_x)_2O_7$ ($0.0 \leq x \leq 1.0$) system. *Chem. Mater.* **2012**, *24*, 4294−4300.
(90) Leszczynska, M.; Liu, X.; Wrobel, W.; Malys, M.; Krynski, M.; Norberg, S. T.; Hull, S.; Krok, F.; Abrahams, I. Thermal variation of structure and electrical conductivity in $Bi_4YbO_{7.5}$. *Chem. Mater.* **2013**, *25*, 326−336.
(91) Norberg, S. T.; Rahman, S. M. H.; Hull, S.; Knee, C. S.; Eriksson, S. G. The proton conducting electrolyte $BaTi_{0.5}In_{0.5}O_{2.75}$: Determination of the deuteron site and its local environment. *J. Phys.: Condens. Matter* **2013**, *25*, 454214.
(92) Keeble, D. S.; Barney, E. R.; Keen, D. A.; Tucker, M. G.; Kreisel, J.; Thomas, P. A. Bifurcated polarization rotation in bismuth-based piezoelectrics. *Adv. Funct. Mater.* **2013**, *23*, 185−190.
(93) Payne, J. L.; Tucker, M. G.; Evans, I. R. From fluorite to pyrochlore: Characterisation of local and average structure of neodymium zirconate, $Nd_2Zr_2O_7$. *J. Solid State Chem.* **2013**, *205*, 29−34.
(94) Kalland, L.-E.; Norberg, S. T.; Kyrklund, J.; Hull, S.; Eriksson, S. G.; Norby, T.; Mohn, C. E.; Knee, C. S. C-type related order in the defective fluorites $La_2Ce_2O_7$ and $Nd_2Ce_2O_7$ studied by neutron scattering and *ab initio* MD simulations. *Phys. Chem. Chem. Phys.* **2016**, *18*, 24070−24080.
(95) Chen, D. P.; Neuefeind, J. C.; Koczkur, K. M.; Bish, D. L.; Skrabalak, S. E. Role of Short-Range Chemical Ordering in $(GaN)_{1-x}(ZnO)_x$ for Photodriven Oxygen Evolution. *Chem. Mater.* **2017**, *29*, 6525−6535.
(96) Diaz-Lopez, M.; Freire, M.; Joly, Y.; Colin, C. V.; Fischer, H. E.; Blanc, N.; Boudet, N.; Pralong, V.; Bordet, P. Local structure and lithium diffusion pathways in $Li_4Mn_2O_5$ high capacity cathode probed by total scattering and XANES. *Chem. Mater.* **2018**, *30*, 3060−3070.
(97) Borowska-Centkowska, A.; Leszczynska, M.; Krok, F.; Malys, M.; Wrobel, W.; Hull, S.; Abrahams, I. Local structure and conductivity behaviour in $Bi_7WO_{13.5}$. *J. Mater. Chem. A* **2018**, *6*, 5407−5418.
(98) Kitamura, N.; Hayashi, N.; Ishida, N.; Idemoto, Y. Local structure in A-site-deficient perovskite $Na_{0.5}Bi_{0.5}TiO_3$ and its effect on electrical conduction. *Chem. Lett.* **2019**, *48*, 1398−1401.
(99) Kitamura, N.; Kubo, Y.; Ishida, N.; Idemoto, Y. Study of atomic ordering across the layer in lithium-rich layered positive electrode material towards preparation process optimization. *J. Power Sources* **2019**, *437*, 226905.
(100) Marlton, F. P.; Nayak, S.; Venkateshwarlu, S.; Chan, N. H.; Kong, J.; Zhang, Y.; Tucker, M. G.; Jørgensen, M. R. V.; Pramanick, A. Broad Distribution of Local Polar States Generates Large Electrothermal Properties in Pb-Free Relaxor Ferroelectrics. *Chem. Mater.* **2021**, *33*, 8844−8853.
(101) Krayzman, V.; Bosak, A.; Playford, H. Y.; Ravel, B.; Levin, I. Incommensurate Modulation and Competing Ferroelectric/Antiferroelectric Modes in Tetragonal Tungsten Bronzes. *Chem. Mater.* **2022**, *34*, 9989−10002.
(102) Miyazaki, R.; Ikeda, K.; Kitamura, N.; Takabayashi, Y.; Kimura, K.; Hayashi, K.; Hihara, T. Reverse Monte Carlo analysis of NaI-LiI solid electrolyte based on the neutron total scattering data. *Mater. Today Commun.* **2022**, *32*, 104014.
(103) Ming, J.; Leszczyńska-Redek, M.; Malys, M.; Wrobel, W.; Jamroz, J.; Struzik, M.; Hull, S.; Krok, F.; Abrahams, I. Dopant clustering and vacancy ordering in neodymium doped ceria. *J. Mater. Chem. A* **2024**, *12*, 10203−10215.
(104) Van Rossum, G.; Drake, F. L. *Python 3 Reference Manual*; CreateSpace: Scotts Valley, CA, 2009.
(105) Ong, S. P.; Richards, W. D.; Jain, A.; Hautier, G.; Kocher, M.; Cholia, S.; Gunter, D.; Chevrier, V. L.; Persson, K. A.; Ceder, G. Python Materials Genomics (pymatgen): A robust, open-source python library for materials analysis. *Comput. Mater. Sci.* **2013**, *68*, 314−319.
(106) Mathon, O.; Beteva, A.; Borrel, J.; Bugnazet, D.; Gatla, S.; Hino, R.; Kantor, I.; Mairs, T.; Munoz, M.; Pasternak, S.; Perrin, F.; Pascarelli, S. The time-resolved and extreme conditions XAS (TEXAS) facility at the European Synchrotron Radiation Facility: The general-purpose EXAFS bending-magnet beamline BM23. *J. Synchrotron Radiat.* **2015**, *22*, 1548−1554.
(107) Kerr, B. V.; King, H. J.; Garibello, C. F.; Dissanayake, P. R.; Simonov, A. N.; Johannessen, B.; Eldridge, D. S.; Hocking, R. K. Characterization of energy materials with X-ray absorption spectroscopy: Advantages, challenges, and opportunities. *Energy & Fuels* **2022**, *36*, 2369−2389.
(108) Newville, M. Larch: An analysis package for XAFS and related spectroscopies. *J. Phys.: Conf. Ser.* **2013**, *430*, 012007.
(109) Perdew, J. P.; Burke, K.; Ernzerhof, M. Generalized gradient approximation made simple. *Phys. Rev. Lett.* **1996**, *77*, 3865.
(110) Blöchl, P. E. Projector augmented-wave method. *Phys. Rev. B* **1994**, *50*, 17953.
(111) Kresse, G.; Furthmüller, J. Efficient iterative schemes for *ab initio* total-energy calculations using a plane-wave basis set. *Phys. Rev. B* **1996**, *54*, 11169.
(112) Kresse, G.; Joubert, D. From ultrasoft pseudopotentials to the projector augmented-wave method. *Phys. Rev. B* **1999**, *59*, 1758.
(113) Monkhorst, H. J.; Pack, J. D. Special points for Brillouin-zone integrations. *Phys. Rev. B* **1976**, *13*, 5188.
(114) Dudarev, S. L.; Botton, G. A.; Savrasov, S. Y.; Humphreys, C. J.; Sutton, A. P. Electron-energy-loss spectra and the structural stability of nickel oxide: An LSDA+ U study. *Phys. Rev. B* **1998**, *57*, 1505.
(115) Das, H.; Urban, A.; Huang, W.; Ceder, G. First-principles simulation of the (Li-Ni-vacancy) O phase diagram and its relevance for the surface phases in Ni-Rich Li-Ion cathode materials. *Chem. Mater.* **2017**, *29*, 7840−7851.
(116) Genreith-Schriever, A. R.; Banerjee, H.; Menon, A. S.; Bassey, E. N.; Piper, L. F. J.; Grey, C. P.; Morris, A. J. Oxygen hole formation controls stability in $LiNiO_2$ cathodes. *Joule* **2023**, *7*, 1623−1640.
(117) Stukowski, A. Visualization and analysis of atomistic simulation data with OVITO-the Open Visualization Tool. *Modelling Simul. Mater. Sci. Eng.* **2010**, *18*, 015012.
(118) Nagle-Cocco, L. A. V.; Steele, J. M. A.; Tacconis, C. *ESRF datsets* **2022**, DOI: 10.15151/ESRF-ES-962076745.
(119) Nagle-Cocco, L. A. V.; Genreith-Schriever, A. R.; Steele, J. M. A.; Tacconis, C.; Bocarsly, J. D.; Mathon, O.; Neuefeind, J. C.; Liu, J.; O' Keefe, C. A.; Goodwin, A. L. et al., University of Cambridge data repository, 2024, DOI: 10.17863/CAM.112349.

(120) Momma, K.; Izumi, F. VESTA 3 for three-dimensional visualization of crystal, volumetric and morphology data. *J. Appl. Crystallogr.* **2011**, *44*, 1272−1276.
(121) Hunter, J. D. Matplotlib: A 2D graphics environment. *Comput. Sci. Eng.* **2007**, *9*, 90−95.

https://doi.org/10.1021/jacs.4c09922
J. Am. Chem. Soc. 2024, 146, 29560−29574